

PHASE RETRIEVAL METHODS FOR SURFACE
CRYSTALLOGRAPHY

By
Ross J. Harder

A Dissertation Submitted in
Partial Fulfillment of the
Requirements for the Degree of

Doctor of Philosophy

in

Physics

at

The University of Wisconsin-Milwaukee

May 2002

PHASE RETRIEVAL METHODS FOR SURFACE
CRYSTALLOGRAPHY

By
Ross J. Harder

A Dissertation Submitted in
Partial Fulfillment of the
Requirements for the Degree of

Doctor of Philosophy

in

Physics

at

The University of Wisconsin-Milwaukee

May 2002

Major Professor

Date

Graduate School Approval

Date

ABSTRACT

PHASE RETRIEVAL METHODS FOR SURFACE CRYSTALLOGRAPHY

by
Ross J. Harder

The University of Wisconsin-Milwaukee, 2002

Under the supervision of Prof. Dilano K. Saldin

The key to understanding, and perhaps more importantly predicting, the detailed properties of materials and surfaces is an accurate model of the atomic structure of the surface. Everything from the flow of current through a transistor in an integrated circuit, to the function of the catalyst in a car's catalytic converter depends on the atomic structure of the surface under consideration.

Determination of the structures of surfaces on an atomic scale is carried out through several experimental methods. In the case of crystal surfaces, diffraction methods are frequently employed. These methods exploit the long-range periodicity of a crystal and the predictable interference of scattered waves due to this periodicity to detect the atomic structure of the material. In these techniques the intensities of the scattered radiation (electromagnetic or particle) are measured although it is in the relative phases of the scattered waves where much of the structural information is contained. Unfortunately the loss of the mostly immeasurable phases leads to time consuming and tedious methods

for analysis of diffraction data which depend on models proposed by the investigator.

The work presented here is a method by which this phase information can be recovered given just the measured intensities and the presumed known, bulk crystalline structure to enable the model-independent determination of the atomic-scale structure of the surface.

This work has been carried out for two different diffraction methods with surface sensitivity. The first is surface x-ray diffraction (SXR) for which the method will be described in detail. The second is the case of low energy electron diffraction (LEED) to which the method developed in the first case will be applied through identification of justifiable analogies between the two techniques. Results from simulated data are presented from several different classes of surface structures.

Major Professor

Date

Acknowledgments

When my advisor, Prof. Dilano Saldin, asked the day before this thesis due to my defense committee if I was going to put a quotation at the front as is sometimes done in these things; my response was that I didn't really know one that I felt was appropriate. His answer to this was something along the lines of "How about 'Brevity is the soul of wit.' " This was both a comment on the relative brevity of this thesis and a quote from Shakespeare. This was also a perfect example of his own wit which has made him such pleasure to have spent the last six years of my life working with. I was amazed by his work, presented in a colloquium, when I was an undergrad and I continue to be amazed by his scientific creativity to this day. Many thanks must go to Prof. Saldin for a thoroughly enjoyable graduate experience.

In the course of the last six years I've had many worthwhile discussions with our resident part-time post-doc Valentin Shneerson. New topics and ideas often mystify each of us in the same way. I've had a lot of fun sorting these things out with him. His contributions to this work are deserving of my deepest thanks.

I feel the thing that makes life as a graduate student truly a life is the camaraderie which you develop with fellow students. Mark Pauli and Dan Giese have been staples in my life for eight years now. In more recent years Demian Cho, Duncan Brown, Steve Blattnig and Ron Gaffney have joined Mark and Dan in making me laugh and soothing my doubts. Hopefully these will turn into life long friendships so we can continue to share in each others successes and failures. Thanks guys.

The Physics Department is not this awful building that they keep us in; it is the people who compose the faculty, staff and students. I've been fortunate to have

interacted with most of them in some fashion. On top of being first class scientists, the faculty is a great collection of people. As an undergraduate at UWM I took the introductory physics classes from Prof. Richard Sorbello. I have to credit him with inspiring me to declare physics as my major. I'm thrilled that he is now on my Ph.D. committee. The rest of my defense committee, save my advisor, has actually been at UWM for a shorter period than me. I owe ym thanks to Prof. Marija Gajdardziska-Josifovska, Prof. Paul Lyman, and Prof. Michael Weinert for having taken time from their busy schedules to read my thesis and contribute to its final form through the defense hearing.

The staff in the physics department is, for the most part, always cheerful and willing to help. One in particular, whom I'm certain has been acknowledged in every thesis of the modern era, is Sue Arthur the department business manager. They credit Copernicus with stopping the Sun and moving the Earth, but everyone in the physics department knows who is really pulling the strings. Thanks for everything Sue.

I've been fortunate to have the influence of four parents in my life. My mom, Sue, and step dad, Gunars, have been my biggest supporters. The words "Thank you" don't really do the feeling justice, but at least it's something tangible in a thesis that really only exists because they are my true parents. My step mom, Nelda, brought a large group of step brothers and sisters into my life, before passing away over nine years ago, to complement my sister Kelley. I often notice bits of Kelley, and the rest, in my personality. They have definitely contributed to making me who I am, and deserve more than the thanks offered here. Given the death of our father less than six months ago, at the time of writing, it's been hard to think of some way to say what I want to say to him.

The thought of dedicating this thesis to him crossed my mind, but I'm not sure I understand what that means. The fact that he never saw it come to completion leaves me with feelings more in tune with sorrow than thankfulness. I am so sorry for all of the time I have wasted in the last year. Nevertheless I think my dad took some pride in the fact that his son was following in his footsteps and adding another Ph.D. to the bookshelf full of family degrees. I promise a copy of mine will be there.

I want to include my newest step parent, Lynda, in this list of people deserving thanks. She hasn't made an impact in my life to the degree that she has a direct responsibility for this work, but she did make my dad's final years something special, and for this I hope mention here is some kind of meaningful thanks. I believe that she is going to be a welcome part of my future, whatever that may be.

TABLE OF CONTENTS

LIST OF FIGURES	ix
Chapter 1: Introduction.....	1
Chapter 2: Surface X-ray Diffraction	8
Chapter 3: Bayes' Theorem and Maximum Entropy Methods.....	15
Chapter 4: Results From Simulated SXRD data.....	29
Chapter 5: Mixed Domain surfaces and Results from SXRD	42
Chapter 6: Extension of MEM to LEED in One Dimension	55
Chapter 7: Summary & Conclusions	67
References.....	73
Vita.....	76

LIST OF FIGURE

1.1	The effect of swapping the phases and amplitudes of the Fourier transforms of two real objects.	3
2.1	Simulated SXR D rod scans from CO/Ni(001).	10
2.2	Reciprocal space geometry of a surface X-ray diffraction experiment.	11
2.3	A one dimensional surface in which the surface unit cell (solid box) has a lower periodicity than that of the bulk unit cell (dashed box).	12
3.1	The prior probability is deduced through the random filing of bins $\{1,2,3,\dots\}$ of specified sizes $\{m_1,m_2,m_3,\dots\}$ by a team of monkeys to produce a distribution $\{u_1,u_2,u_3,\dots\}$ of objects.	19
3.2	An amplitude-phase diagram showing a known complex bulk amplitude, B_q , and the known modulus of the experimental amplitude which must lie somewhere on the circle shown.	23
3.3	A flow chart of the MEM algorithm.	25
4.1	The diffraction pattern of the Cu(104) surface.	29
4.2	The geometry of a two dimensional centered unit cell.	30
4.3	The initial electron density distribution obtained by applying the phases of the bulk unit cell	31
4.4	The final electron density distribution recovered for O/Cu(104)-1x1.	32
4.5	Side view of the final O/Cu(104)-1x1 surface electron density distribution.	32
4.6	Top view of the final O/Cu(104)-1x1 surface electron density distribution.	32
4.7	R-factor versus iteration number for recovery of O/Cu(104) surface density.	33
4.8	The asymmetric unit of the diffraction pattern from GaAs(111)-2x2.	34
4.9	The initial surface electron density distribution used to begin recovery of the GaAs(111)-2x2 surface structure.	35
4.10	The 1x1 averaged surface electron density distribution of GaAs(111)-2x2.	36
4.11	The final electron density distribution obtained for GaAs(111)-2x2.	37

4.12	The R-factor as a function of iteration for the recovery of GaAs(111)-2x2.	38
4.13	Top view of the density recovered for GaAs(111)-2x2.	38
4.14	Super-resolution for O/Cu(104).	40
5.1	An illustration of a surface with two domains which are rotated with respect to each other.	43
5.2	The (2x2) unit cell used in the simulation of data from two domains.	44
5.3	Diffraction pattern from Ge(001)-2x1 in a 2x2 mesh with two domains at right angles to each other.	45
5.4	The initial surface electron density distribution, for recovery of our hypothetical Ge(001)-2x1 two domain structure.	46
5.5	The averaged 1x1 surface electron density distribution of our model for Ge(001)-2x1 with two domains for which the scattered amplitudes have been added coherently.	46
5.6	The final electron density distribution recovered upon inclusion of the superstructure rods from Ge(001)-2x1.	47
5.7	The R-factor as a function of iteration number during the recovery of Ge(001)-2x1 from coherently added scattering amplitudes from two domains.	48
5.8	The initial surface electron density distribution used for the recovery of the structure Ge(001)-2x1 from incoherently averaged SXRD intensities of two domains.	49
5.9	The averaged 1x1 surface electron density distribution of our model for Ge(001)-2x1 with two domains for which the scattered amplitudes have been added incoherently.	50
5.10	The final electron density distribution recovered from incoherently averaged domains upon inclusion of the superstructure rods from Ge(001)-2x1.	50
5.11	The R-factor as a function of iteration number during the recovery of Ge(001)-2x1 from incoherently added scattering amplitudes from two domains.	51
5.12	Diffraction pattern from TiO ₂ (001)-c2x2 with two domains mirrored with respect to one another.	52

5.13	The initial electron density given to the algorithm for the recovery of K/TiO ₂ from two incoherently averaged domains.	53
5.14	The final electron density distribution recovered from incoherently averaged intensities from two domains of a hypothetical (c2x2)-K/TiO ₂	53
5.15	The R-factor, as a function of iteration number, for the recovery of a hypothetical model for K/TiO ₂ in mirrored domains which have been incoherently averaged. ...	54
6.1	Representation of the electron propagation and scattering paths.....	60
6.2	Solid line: calculated LEED intensity vs. energy for the specular, or (00) beam from a (c2x2)-CO/Ni(001) surface. Dashed line: calculated LEED intensity vs. energy for the same beam from a clean Ni(001) surface with the same electron absorption parameters.	63
6.3	Evolution of the one-dimensional distribution of atomic scatters as calculated by our algorithm as a function of height above the outermost later of Ni atoms of the substrate.	66

Chapter 1: Introduction

“Why surfaces?”, to quote the first line of the first chapter of Woodruff & Delchar [Wo94]. In a very real sense the answer is, “Because that’s where the action is.” The reason for this is likely to be quite obvious; for the most part materials interact with other entities at their surfaces. Also, if we wish to shape a material to be of use to us, it is ultimately the surface with which we work. From integrated circuits etched onto the surface of a semiconductor crystal to the platinum metal in the catalytic converter of most cars, it is the surface properties of the material in use that makes it suitable for the application.

The atomic-scale structure of the surface of a solid can be extremely different from that of the bulk. These structural differences can lead to significantly different electronic and vibrational properties in the surface region. In turn these properties play a major role in determining the behavior of the surface in technological applications. In order to understand, and more importantly predict, these fundamental physical properties of the surface, the atomic scale structure of the surface needs to be known [Wo94].

There are many experimental techniques from which the structural properties of the surface can be garnered. In general they can be split into three groups; microscopy, spectroscopy, and scattering or diffraction techniques [Wo94]. Microscopy essentially “looks” directly at the surface. Whether light or particles are used as the observational probe, direct information is given about the structure of the surface. Included in this group are techniques like transmission electron microscopy (TEM) and scanning tunneling microscopy (STM). Spectroscopic techniques commonly involve energy-analyzing the particles that are the probe of the technique; often these are electrons. One

commonly used spectroscopic technique is x-ray absorption near edge spectroscopy (XANES). This technique is particularly useful for chemical fingerprinting the unknown components on a surface. In XANES the shape, or structure, of the absorption curve of x-rays is studied near the absorption edge of a particular atomic species. The shape of the spectroscopic curve near the absorption edge is characteristic of the atomic environment in the vicinity of the absorbing atom. The analysis of XANES data can be difficult. The common method is to make an educated guess of the local atomic structure of the absorber and use computer simulation of the experimental XANES data to test the validity of the guess. Iterations of modification and simulation can eventually lead to a satisfactory model for at least a portion of the surface [Wo94]

The focus of this work is the analysis of diffraction techniques, in particular those of surface x-ray diffraction (SXRD) [Ro92] and low energy electron diffraction (LEED) [Va79]. Traditional analysis of diffraction data is much the same as that mentioned above for XANES. A test structure is concocted and used as input for a simulation of the experimental intensities. Modifications are made to the test structure, either through intuition or some algorithm, and then another simulation is performed. Iterations of modification and simulation can eventually result in a model for the structure. This can be a long and laborious task, even if the atomic species and the number of each composing the surface unit cell are known [Pe88].

The difficulties encountered in conventional analysis have spurred the development of what have been termed *direct methods* for structure determination from diffraction data [Gia80,Pe88,Sa52,Br84,Br88,Br91]. Since only the diffracted intensities of waves, and not their relative phases, are accessible from experiment the simple

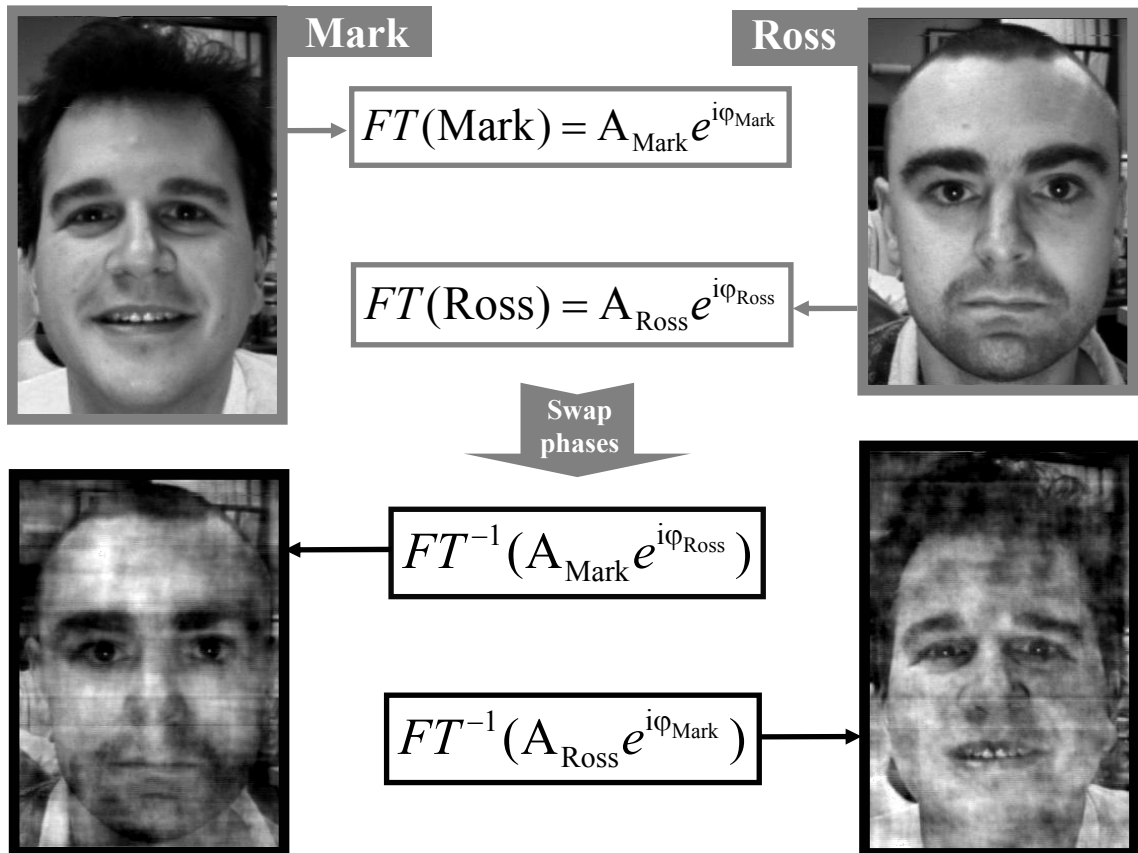


Figure 1.1 The effect of swapping the phases and amplitudes of the Fourier transforms of two real objects. The inverse Fourier transform more closely resembles the image from which the phases were derived.

inversion, via a Fourier transform, of the scattered amplitudes is not possible. Many algorithms have been developed to retrieve the phase information lost in the experimental measurement. This problem is not unique to surface crystallography; in fact the identical problem exists in macromolecular crystallography, radio astronomy and image analysis [Ja57,Co82,Fi78,Fi82,Sh01]. We have borrowed from all of these fields in the development of a direct method for application to surface crystallography.

We begin with a simple but graphic example illustrating the importance of the phases in any experiment where a real object is sought from the amplitudes of its Fourier transform. Figure 1.1 shows monochrome photographs of my office mate (Mark Pauli) and me (Ross Harder). A fast Fourier transform (FFT) of the rectangular array of

numbers representing the digitized versions of these photographs may be performed to yield a corresponding array of complex amplitudes.

The results of the inverse Fourier transforms of these amplitudes with the phases and amplitudes interchanged is shown in the lower panels of Figure 1.1. It is quite striking that the most recognizable features of the two images returned are those of the original image from which the *phases* of the scrambled amplitudes are derived. A similar demonstration by Read [Re97] reached the same conclusion. It is certainly necessary to recover the lost phases of the measured amplitudes if we wish to directly determine the structure of the surface.

Borrowing from several methods which have become the cornerstones of direct methods in various fields, an algorithm will be developed in this thesis for application to SXRD. We begin by identifying the measured intensities in SXRD as the modulus squared of an *object wave* arising from scattering by the unknown surface of the crystal coherently summed with a *reference wave* arising from the presumed known bulk of the crystal [Sz93]. This is in contrast with holographic LEED [DKS90][He01] where the reference wave is regarded as that scattered by an adatom and the object wave as the part of this wave subsequently scattered by the substrate. LEED holography most recently has been an aid in the determination of the structure of SiC(111)-3x3 [Reu97]. The technique was able to determine the structure of a local five atom cluster in the vicinity of a prominent adatom. Due to the one upon r decay of the amplitudes of spherical electron wave functions, which form the reference wave in the method, only a cluster of atoms in the vicinity of the reference scattering atom can be recovered [DKS97]. The holographic

analysis took only a matter of hours, but the determination of the remainder of the unit cell took a further half of a year through conventional trial and error methods.

Our holographic interpretation makes the problem of determining the structure of a surface formally identical to the structure completion problem encountered in protein crystallography. Often a portion of a protein can be determined through other means. This known portion can then be thought of as giving rise to a reference wave which can be of use in the determination of the remainder of the structure.

The earliest approximate method for solution of the structure completion problem, in protein crystallography, to estimate the unknown phases is the *unweighted difference Fourier* method [Coc51], which approximates the phases of the total structure factors by those of the known part of the structure. In the case of surface crystallography the known part of the structure is just that of the bulk of the crystal. The algorithm we have developed uses this as the starting point for a further refinement.

The Gerchberg-Saxton algorithm was one of the first iterative methods for the recovery of the crystallographic phases [Gs71]. It functions through the imposition of constraints in both real and reciprocal space. In the x-ray crystallography case the electron density is constrained to some physically reasonable volume of real space (a support constraint), and in reciprocal space the amplitudes are constrained to the experimentally measured values, with the phases set to those obtained from the Fourier transform of the constrained density. This notion of alternating back and forth between real and reciprocal space on successive iterations, satisfying known constraints in each, will be the framework upon which we build our algorithm.

Fienup later generalized the algorithm of Gerchberg and Saxton into a class of input-output algorithms [Fi78,Fi82]. All of these impose essentially the same constraint in reciprocal space, applying estimated phases obtained through the Fourier transform, to the measured amplitudes. In real space they include a variety of constraints. These range from a simple imposition of a support constraint and *positivity* (or non-negativity) to more sophisticated methods for mixing old and new estimates of the real space function (the electron density in the SXR D case).

The work of Collins [Co82] fits the concept of constrained entropy maximization into the framework of the input-output type algorithm. From elementary statistical physics it is known that the probability of a system being in a state characterized by a set of parameters is proportional to the exponential of the entropy of the system [Rei65]. The entropy to be maximized in our case is that of the electron density distribution in real space; this of course must be constrained by the fact that the electron density obtained is consistent with that which produced the measured data. Collins applied entropy maximization to the refinement of phases in protein crystallography. It is common to modify a protein through isomorphous replacement and repeat diffraction measurements. Usually heavy atoms are used, which affect the phases of the reflections in a predictable way. Many such replacements can allow the prediction of the phases of the measured reflections of the unmodified protein with some certainty. The goal of Collins' work was to start with these estimated phases and produce an even better density map of the protein through the constrained maximization of the entropy of the map. This work was based on that of Gull and Daniel [GD78] who focused upon a similar problem in radio astronomy.

The algorithm will be derived in a later chapter through the rules of deductive logic [Si96] and information theory [Ja57].

In this dissertation the work of Collins, Fienup, Gerchberg and Saxton, and Cochran will be combined with the holographic interpretation of the data to develop an iterative algorithm for solution of the structure completion problem in surface crystallography. The algorithm developed will be tested on simulated SXRD data from several types of model surface structures. Although this algorithm is developed with SXRD data in mind, it has been adapted to LEED by making appropriate analogies between the two experimental methods. The tools used to derive the algorithm are based in probability theory and deductive logic. Bayes theorem [Si96] is our starting point, with justifiable assignments of probability made in the context of our problem of obtaining the most likely electron density distribution of the surface unit cell, given the experimental data and known bulk structure.

Chapter 2: Surface X-ray Diffraction

Given that the x-ray scattering cross section for atoms is so small, on the order of 10^{-6} \AA^2 , x-rays were thought to penetrate too far into the solid to be sensitive to surface features. With the advent of very bright synchrotron x-ray sources and more sensitive diffractometers, surface x-ray diffraction (SXRD) experiments have become possible [Wo94].

The basic unit of scattering for x-rays in a solid is the electron. In the case of SXRD experiments the kinematical, classical theory of x-ray scattering is sufficient. The task of calculating the scattering amplitudes for the atoms that make up a solid is a simple matter of integrating the appropriate scattering amplitude for a single electron over the electron density of the atom. Fortunately, the scattering factors for most atoms have been calculated and are tabulated in the International Tables for X-ray crystallography [ITXRD74]. A more convenient, parameterized, form of the atomic scattering factor is also available from the International Tables, given by

$$f\left(\frac{\sin\theta}{\lambda}\right) = \sum_{i=1}^4 a_i \exp(-b_i \left(\frac{\sin\theta}{\lambda}\right)^2) + c . \quad (2.1)$$

Where the parameters a_i , b_i and c are known for most atoms. θ is the scattering half angle and λ is the wavelength of the x-ray. The quantity $\sin(\theta)/\lambda$ can be shown to be equal to $|\mathbf{q}|/2$, half of the magnitude of the momentum transfer vector $\mathbf{q}=\mathbf{k}-\mathbf{k}_0$, where \mathbf{k}_0 is the incident x-ray momentum and \mathbf{k} is the scattered x-ray momentum. In SXRD it is only the elastically scattered x-rays that are of importance, therefore the magnitudes of \mathbf{k}_0 and \mathbf{k} are identical. The atomic scattering factor is the ratio of the amplitude of radiation scattered by an atom to that scattered by a single electron.

The intensities that are measured in an SXR experiment are, in the simplest case, given by

$$I_{\mathbf{q}}^{Exp} = |F_{\mathbf{q}}^{Exp}|^2 = |B_{\mathbf{q}} + S_{\mathbf{q}}|^2, \quad (2.2)$$

where $F_{\mathbf{q}}^{Exp}$ represents the total structure factor from the experiment [VI98]. $B_{\mathbf{q}}$ is the contribution from the truncated bulk crystal given by

$$B_{\mathbf{q}} = \sum f_j(\frac{q}{2}) \exp(-\frac{B_j q^2}{16\pi^2}) \exp(2\pi i \mathbf{q} \cdot \mathbf{r}_j) \frac{1}{1 - \exp(-2\pi i L) \exp(-\alpha)}. \quad (2.3)$$

Eq.(2.3) is similar to the x-ray structure factor defined in solid state physics. It is a sum over the atoms in the unit cell with appropriate scattering factors f_j , and phase factors $\exp(2\pi i \mathbf{q} \cdot \mathbf{r}_j)$, as well as Debye-Waller factors $\exp(-\frac{B_j q^2}{16\pi^2})$ and possibly surface roughness corrections (not included in (2.3)) [VI98]. The part that is unique to SXR is the term

$$\frac{1}{1 - \exp(-2\pi i L) \exp(-\alpha)}, \quad (2.4)$$

which allows a continuous intensity as a function of Miller index L , the index that specifies the component of momentum transfer perpendicular to the surface. This term arises due to the truncation of the 3D crystal, and the subsequent breaking of the periodicity to form the surface. The contribution of the bulk to $F_{\mathbf{q}}^{Exp}$ is inherently taken to be that from a perfectly flat, perfectly terminated bulk crystal. All variation of the diffraction intensity from that produced by the perfectly terminated bulk surface is presumed to arise from the region denoted here as the surface. It is to the continuous intensity distribution, between the Bragg peaks at integer values of L , that the surface unit cell contributes measurably. The component $\exp(-\alpha)$ in eq. (2.4) is an attenuation factor

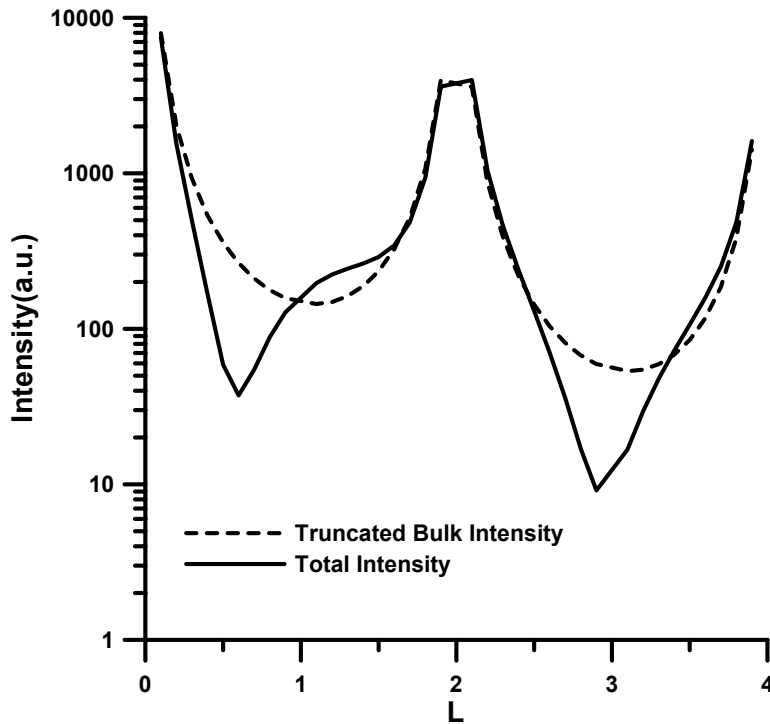


Figure 2.1 Simulated SXRD rod scans from CO/Ni(001)-1x1. Shown are the intensities as a function of the miller index L for the total surface, including both the bulk and surface unit cell (solid line), and for just a bulk terminated Ni surface (dashed line). Both are for $H=0$ and $K=0$.

which depends on the composition of the bulk of the crystal [V198]. The surface contribution to eq. (2.2) is given by

$$S_{\mathbf{q}} = \sum f_j(\frac{q}{2}) \exp(-\frac{B_j q^2}{16\pi^2}) \exp(2\pi i \mathbf{q} \cdot \mathbf{r}_j) \quad (2.5)$$

with many of the same terms as the scattering factor of the bulk only now the summation is over the atoms of the surface unit cell [V198]. In our terminology the surface unit cell is composed of any surface layers which do not compose a complete bulk unit cell. This includes any additional layers of reconstructed or relaxed bulk species as well as adsorbed atomic species.

The simulated SXRD crystal truncation rods shown in Figure 2.1 illustrate the surface sensitivity of the technique [V100]. Near the Bragg spots at integer values of L

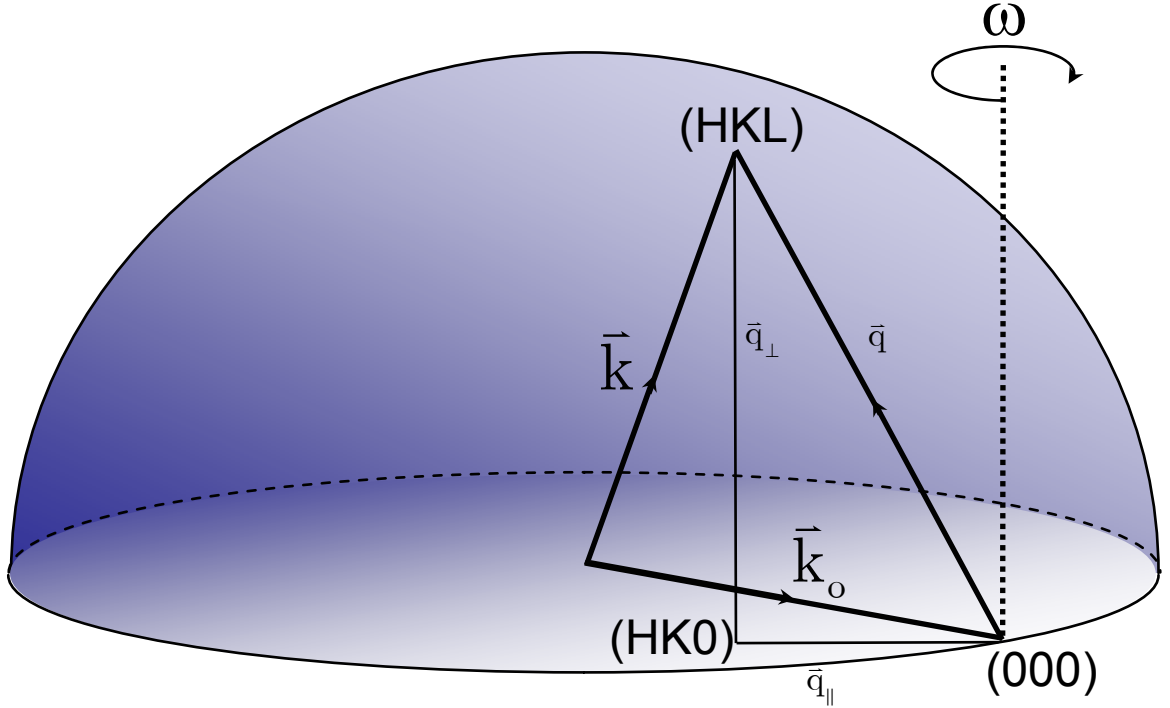


Figure 2.2 Reciprocal space geometry of a surface X-ray diffraction experiment.

the intensity from the total surface differs only slightly (in traditional terms) compared to the bulk terminated crystal, but in the continuous intensity distribution between the Bragg spots the difference is significant.

Figure 2.2 shows the geometry of the SXRD experiment in reciprocal space. The incident x-ray, with wave vector \mathbf{k}_o , is at a glancing angle to the surface. The diffracted x-ray, with wave vector \mathbf{k} , must lie on the Ewald sphere and must satisfy the diffraction condition for its parallel component given by Bragg's Law

$$\mathbf{q}_{\parallel} = \mathbf{g} = H\mathbf{a}^* + K\mathbf{b}^* . \quad (2.6)$$

Eq. (2.6) simply states that the component of the momentum transfer vector \mathbf{q} parallel to the surface must be a reciprocal lattice vector, where \mathbf{a}^* and \mathbf{b}^* are reciprocal space unit vectors. This condition leads to a set of diffraction spots denoted by the Miller indices H and K for any given perpendicular component denoted by Miller index L . The

perpendicular component is not restricted by the diffraction condition given in eq.(2.6) due to the lack of periodicity perpendicular to the surface. The intensity variation as a function of L corresponding to values of H and K not forbidden by the substrate lattice is known as a crystal truncation rod (CTR). The variation as a function of L is accessed, in figure 2.2, by rotating the Ewald sphere about the point labeled (000). As a result of this rotation the perpendicular component of \mathbf{q} will intersect the sphere at the continuum of values which compose the CTR. To obtain intensities in the specular rod, $H=0$ and $K=0$, the Ewald sphere needs to be tipped such that the sphere intersects the (00) rod. The rotations of the Ewald sphere are accomplished in the experiment by manipulating the sample orientation as well as the detector orientation with respect to the sample.

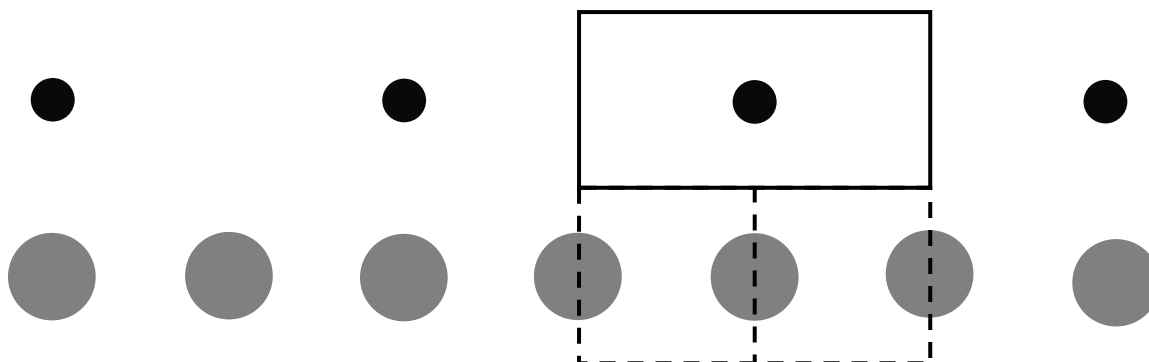


Figure 2.3 A one dimensional surface in which the surface unit cell (solid box) has a lower periodicity than that of the bulk unit cell (dashed box).

In practice the 2D periodicity of the surface unit cell can be larger than the periodicity of the bulk in a direction parallel to the surface. This situation gives rise to so called superstructure spots. These are diffraction spots that have only contribution from the surface unit cell and lie in between the CTRs of the bulk two-dimensional reciprocal mesh. The following 1D example illustrates the existence of the superstructure spots.

Figure 2.3 shows a one dimensional crystal: the larger lighter colored “atoms” in the figure are the top layer of the bulk; the surface unit cell is composed of the smaller

darker atoms. The periodicity of the surface is half that of the bulk or the surface unit cell is twice as big. Evaluating eq. (2.3) at $L=0.0$ for the coordinates of the atoms in the bulk unit cell gives

$$B_H = f_b(H)(e^{-2\pi i H \cdot 0} + e^{-2\pi i H \cdot 1/2}) \frac{1}{1-\exp(-\alpha)} = f_b(H)(1 + e^{-\pi i H}) \frac{1}{1-\exp(-\alpha)}, \quad (2.7)$$

where the coordinates have been specified as fractions of the surface unit cell length, $x_1=0$ and $x_2=1/2$, and it is assumed that there is only one type of atom in the bulk and the Debye parameters are ignored. From eq. (2.7) it is evident that the scattering amplitude of the bulk will only be non-zero when the Miller index H takes on even values. A similar evaluation of the surface unit cell's structure factor gives, at $L=0.0$,

$$S_H = f_s(H)e^{2\pi i H \cdot 1/2} \quad (2.8)$$

for the sole atom in the surface unit cell at $x=1/2$. The surface unit cell amplitude will have a contribution for all values of H , both even and odd. The odd values of H will be the superstructure spots for this 1D crystal. The superstructure spots will also have a continuous intensity variation as a function of Miller index L , but there will be no Bragg spots at integer values of L , since there is only one layer of the surface unit cell.

Throughout this dissertation the diffraction spots will be indexed with respect to the surface unit cell. This is in contrast to the conventional indexing where the bulk unit cell is taken as the reference lengths, leading to the superstructure spots having fractional indices.

A widely used computer code for the simulation and conventional analysis of SXR data was written by E. Vlieg [Vl00] and is named ROD. We have developed our own SXR simulation code based on that of Vlieg's. There are two reasons for this work; the first being the desire to easily integrate the calculation of the diffraction

amplitudes of the bulk terminated crystal into the programs based on the algorithm described in the following chapters. This is really only possible if the simulation code is written in the form of a subroutine which can be easily called by the main program. Vlieg's code is a self contained program, meant to be run independent of other software. The second reason to rewrite the SXR D simulation code is due to the sensitivity of this calculation to the precision with which the coordinates of the atoms are specified. It is not uncommon for the sum over the atoms of a bulk unit cell to include forty or more independent atoms. Due to rounding errors in the specification of the atomic coordinates involved in these summations it is also not uncommon to get errors in the simulated intensities on the order of 1% from Vlieg's program. While this error is negligible when analyzing noisy experimental data, we have taken the opportunity to improve the structure factor calculation by paying particular attention to the precision with which the atomic coordinates are stored and used in the calculation. This new code produces symmetrically equivalent reflections in agreement to at least eight decimal places. Also, due to the translational symmetry of some crystals, there are structure factors which must be zero. Our new SXR D code produces structure factors for these reflections that are zero to at least twenty decimal places.

Chapter 3: Bayes' Theorem and Maximum

Entropy Methods

The loss of the phases associated with the measured amplitudes $|F_{\mathbf{q}}^{Exp}|$ makes the structure completion problem for SXRD data a problem of inference. The goal is to infer the most probable surface electron density distribution given the measured amplitudes $|F_{\mathbf{q}}^{Exp}|$.

Central to the business of inference is the concept of conditional probability [Si96]. The use of conditional probabilities allows one to assign the probability of an event given knowledge that may determine that probability. An example of this idea is the probability that you may assign to seeing a rainbow at any given instant. This probability is greatly affected by the weather conditions and perhaps the time of day. Given it's a bright sunny day the probability of seeing a rainbow is close to zero. Given that there is rain in the area and that the sun is close to the horizon and not behind the clouds, the probability that you may see a rainbow is significant. Probabilities of this type are denoted $prob(X|I)$ and read as “the probability that X is true given the proposition I is true. In the above example X is the event that there is a rainbow, and I is the information that it is either a bright sunny day or raining in the east with the sun low in the sky to the west. Given the definition of probability as the degree to which we believe something to be true, there is no such thing as an absolute probability. The conditional probability is just the explicit statement of the background information that was used in the assignment of a probability [Si96].

Two important rules are obeyed by probabilities. The first is known as the sum rule:

$$\text{prob}(X | I) + \text{prob}(\bar{X} | I) = 1 \quad (3.1)$$

It is the simple statement that the probability that X is true given I plus the probability that X is false, denoted \bar{X} , given I must be unity [Si96]. As an example, the probability there is a rainbow and it is sunny plus the probability there is not a rainbow and it is sunny must be one.

The product rule is written:

$$\text{prob}(X, Y | I) = \text{prob}(X | Y, I) \times \text{prob}(Y | I) \quad (3.2)$$

It is a statement of the concurrent probability of both X and Y being true [Si96].

Following the theme above, suppose X is the proposition that there will be a rainbow at 2:30pm and Y the proposition that you will be outside to see it at 2:30pm. The probability that you will be outside at 2:30 independent of the existence of a rainbow, $\text{prob}(Y|I)$, multiplied by the probability $\text{prob}(X|Y,I)$ of there being a rainbow at 2:30 given that you are outside to see it, will result in the probability that you will see a rainbow at 2:30pm. Again, all of the probabilities are conditional on relevant background information concerning the propositions. If you are a construction worker on a road crew, for example, the probability that you are outside at 2:30pm is much larger than if you are a graduate student buried in an office with no windows.

From the product rule an important result can be obtained. Recognizing that the $\text{prob}(X, Y | I) = \text{prob}(Y, X | I)$ and applying the product rule to both sides one obtains:

$$\text{prob}(X | Y, I) = \frac{\text{prob}(Y | X, I) \times \text{prob}(X | I)}{\text{prob}(Y | I)}, \quad (3.3)$$

after dividing both sides by $prob(Y|I)$. The resulting expression is known as Bayes' Theorem [Si96]. In the context of inferring the most probable surface electron density given a set of measured SXRD intensities, Bayes' theorem takes the following form:

$$prob(u | "data", I) = \frac{prob("data" | u, I) \times prob(u | I)}{prob("data" | I)} \quad (3.4)$$

Where we have identified proposition X with the surface electron density distribution u , Y with the SXRD "data" and of course I is any background information we have about the electron density distribution. The quantity I can include details such as the fact that the electron density is positive and also the roughly known thickness (a support constraint) of the surface unit cell, as well as any *a-priori* information.

The LHS of (3.4) may be regarded as the *posterior probability* of the electron density given the experimental data and background information. The first term in the numerator on the RHS is known as the *likelihood function* of the data for a given model of the electron density and the background information, and the second term in the numerator the *prior probability* of the electron density given the background information only. The denominator on the RHS is known as the *evidence*. For our problem the last-named quantity may be taken as constant, implying that all measured data is to be treated on an equal footing, and not biased by any background information. In practice this term could permit us to treat data obtained from different experimenters with a different level of confidence; disregarding this complication under the assumption we will work with just one experimenter eq.(3.4) reduces to:

$$prob(u | "data", I) \propto prob("data" | u, I) \times prob(u | I) \quad (3.5)$$

The electron density that maximizes the probability in the LHS of (3.5) is what is sought in X-ray crystallography. The above expression indicates that it is proportional to the product of the likelihood function and the prior probability of that electron distribution.

The likelihood function may be determined by the following argument: given an estimate σ_q of the standard deviation of the error in the experimental measurement of a structure factor amplitude F_q^{Exp} , the probability of such a measurement for a given model of the structure with calculated amplitude F_q^{Calc} is given by the Gaussian distribution:

$$prob(F_q^{Exp} | u, I) = \frac{1}{\sigma_q \sqrt{2\pi}} \exp \left\{ -\frac{|F_q^{Exp} - F_q^{Calc}|^2}{2\sigma_q^2} \right\}. \quad (3.6)$$

Given the multiplicative nature of independent probabilities, it follows that the likelihood function for the entire set of measured data is given by:

$$prob("data" | u, I) = prob(\{F_q^{Exp}\} | u, I) \propto \exp \left\{ -\frac{\chi^2}{2} \right\} \quad (3.7)$$

where

$$\chi^2 = \sum_q \frac{|F_q^{Exp} - F_q^{Calc}|^2}{\sigma_q^2}. \quad (3.8)$$

This “chi-squared statistic” [Si96] could be regarded as another form of R-factor. The modulus of F_q^{Exp} is the square root of the measured intensity. From the definition of the standard deviation σ_q , the minimum expected value of χ^2 would be of the order of the number of terms in the sum (3.8).

Eq.(3.7) shows that minimization of this R-factor is equivalent to maximizing the likelihood function. Eq. (3.5) shows, although this may be the standard practice in conventional trial-and-error structure determinations, the R-factor is only one element in

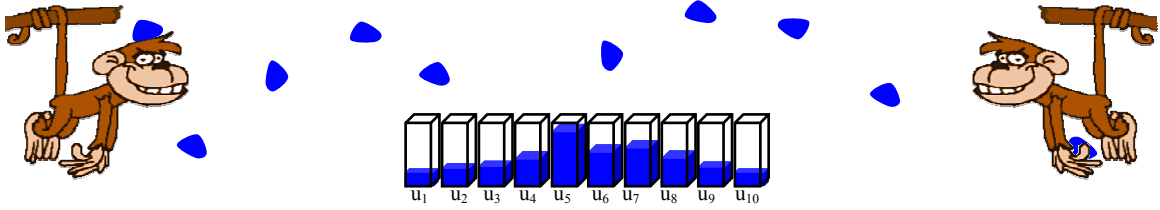


Figure 3.1 The prior probability is deduced through the random filling of bins $\{1,2,3,\dots\}$ of specified sizes $\{m_1,m_2,m_3,\dots\}$ by a team of monkeys to produce a distribution $\{u_1,u_2,u_3,\dots\}$ of objects.

the correct determination of a structure from a given set of measured data. It is necessary also to take account of the prior probability.

The prior probability of the electron distribution is simply the probability of the distribution given the background information, which is, in this case, just the positivity of the electron density and any prior estimate of that distribution on, for example, chemical grounds. Any known periodicity allows attention to be confined to the electron distribution within a repeat unit (or unit cell). The *a priori* probability of such a distribution is analogous to the probability $prob(u|I)$ that a hypothetical team of monkeys (our archetypal unbiased individuals shown in Figure 3.1) throw objects at random into a set of boxes 1, 2, 3, ... of capacities m_1, m_2, m_3, \dots to produce a distribution, u_1, u_2, u_3, \dots of those objects. The distribution $\{m_i\}$ is how we encode some our previous knowledge I of the electron density.

From the standard combinatorial argument [Si96],

$$prob(\{u_i\} | I) \propto \Omega = \prod_i m_i^{u_i} / \prod_i u_i!, \quad (3.9)$$

where Ω is the number of ways the distribution may come about. From Boltzmann's relation, the entropy, S , of the distribution may be written

$$S = \alpha \ln(\Omega), \quad (3.10)$$

where α is a constant. Combining Eqs. (3.9) and (3.10), we may write the prior probability as

$$\text{prob}(\{u_i\} | I) \propto \exp(S / \alpha). \quad (3.11)$$

In the crystallographic application, the quantities u_i are identified with the number of electrons in voxel (or “volume pixel”) associated with a point i of a uniform grid within a unit cell. Thus the distribution $\{u\}$ is proportional to the surface electron density distribution that crystallographers seek to determine. The distribution $\{m\}$ may be regarded as a prior estimate of $\{u\}$ based on the background information alone.

Combining Eqs.(3.5), (3.7), and (3.11), we find that the posterior probability may be written as

$$\text{prob}(\{u_i\} | \text{"data"}, I) \propto \exp\left(\frac{S}{\alpha} - \frac{1}{2} \chi^2\right) \quad (3.12)$$

The most likely electron density distribution consistent with the experimental data and the background information is that which maximizes the exponent on the RHS of (3.12), or equivalently (since α is arbitrary), the functional, $Q[\{u_i\}]$, where:

$$Q[\{u_i\}] = S[\{u_i\}] - \frac{\lambda}{2} \chi^2[\{u_i\}]. \quad (3.13)$$

Regarding λ as a Lagrange multiplier, we see that the problem of finding the most likely electron density consistent with the data may be reduced to that of finding the distribution of maximum entropy constrained by the requirement of minimizing the “chi-squared” statistic. This is exactly the procedure of the maximum entropy method (MEM) of Jaynes [Ja57].

The MEM has been applied to the problem of improving the initial “experimental” estimate of a set of phases of Bragg reflections, in macromolecular

crystallography by Collins [Co82]. Here we follow the derivation of Collins in the application of MEM to SXR. D.

From Eqs. (3.9) and (3.10), and using Stirling's approximation:

$$\ln(u!) = u \ln(u) - u, \quad (3.14)$$

the entropy term in (3.13) may be written as

$$S = -\sum_i u_i \ln(u_i / em_i). \quad (3.15)$$

Writing

$$F_{\mathbf{q}}^{Calc} = B_{\mathbf{q}} + \sum_i u_i \exp(i\mathbf{q} \cdot \mathbf{r}_i) \quad (3.16)$$

substituting (3.16) and (3.8) into (3.13), and taking $\sigma_{\mathbf{q}}=1$ for all \mathbf{q} (for theoretical "data") yields

$$Q[\{u_i\}] = -\sum_i u_i \ln\left(\frac{u_i}{em_i}\right) - \frac{\lambda}{2} \sum_{\mathbf{q}} \left| |F_{\mathbf{q}}^{Exp}| \exp(i\phi_{\mathbf{q}}) - B_{\mathbf{q}} - \sum_i u_i \exp(i\mathbf{q} \cdot \mathbf{r}_i) \right|^2, \quad (3.17)$$

where $\phi_{\mathbf{q}}$ is an estimate of the phase of the measured structure factor $F_{\mathbf{q}}^{Exp}$ and $B_{\mathbf{q}}$ is the known contribution by the bulk of the crystal. According to the theory developed above, the most probable electron distribution consistent with the experimental data $|F_{\mathbf{q}}^{Exp}|$ is that which maximizes the functional Q . We will derive an iterative algorithm for determining this distribution by writing the n -th estimate of this distribution as $\{u_i^n\}$ and identifying $\{m_i\}$ with its estimate $\{u_i^{n-1}\}$ at the previous iteration [Co82]. Thus we re-write (3.17) as

$$Q[\{u_i^n\}] = -\sum_i u_i^n \ln\left(\frac{u_i^n}{eu_i^{n-1}}\right) - \frac{\lambda}{2} \sum_{\mathbf{q}} \left| |F_{\mathbf{q}}^{Exp}| \exp(i\phi_{\mathbf{q}}^{n-1}) - B_{\mathbf{q}} - \sum_i u_i^n \exp(i\mathbf{q} \cdot \mathbf{r}_i) \right|^2, \quad (3.18)$$

where, for $n > 1$,

$$\phi_{\mathbf{q}}^{n-1} = \arg \left(B_{\mathbf{q}} + \sum_i u_i^{n-1} \exp(i\mathbf{q} \cdot \mathbf{r}_i) \right). \quad (3.19)$$

The distribution $\{u_i^n\}$ that maximizes Q is obtained by setting

$$\frac{\partial}{\partial u_i^n} \mathcal{Q}[\{u_i^n\}] = -\ln \left(\frac{u_i^n}{u_i^{n-1}} \right) - \lambda (u_i^n - t_i^{n-1}) = 0 \quad (3.20)$$

for all i , where

$$t_i^{(n-1)} = \frac{1}{N} \sum_{\mathbf{q}} \left\{ |F_{\mathbf{q}}^{\text{exp}}| \exp(i\phi_{\mathbf{q}}^{(n-1)}) - B_{\mathbf{q}} \right\} \exp(-i\mathbf{q} \cdot \mathbf{r}_i) \quad (3.21)$$

and the sum over \mathbf{q} includes Friedel pairs to ensure that t_i^{n-1} is real. Eq.(3.20) may be re-written

$$u_i^n = u_i^{n-1} \exp \left\{ -\lambda (u_i^n - t_i^{n-1}) \right\}, \quad (3.22)$$

which is an implicit equation for u_i^n . This can be converted into an explicit recursion relation for the same quantity by replacing u_i^n on the RHS by u_i^{n-1} . This is justified if λ is chosen small enough that

$$\delta u_i^n \ll |u_i^n - t_i^{n-1}|, \quad (3.23)$$

where

$$\delta u_i^n = u_i^n - u_i^{n-1}. \quad (3.24)$$

Note that if λ were small enough it would be possible also to truncate the series expansion of the exponential on the RHS of (3.22) to approximate this equation by

$$\delta u_i^n = -\lambda u_i^{n-1} \{u_i^n - t_i^{n-1}\}, \quad (3.25)$$

from which it follows that condition (3.23) is equivalent to the requirement that

$$|\lambda u_i^{n-1}| \ll 1. \quad (3.26)$$

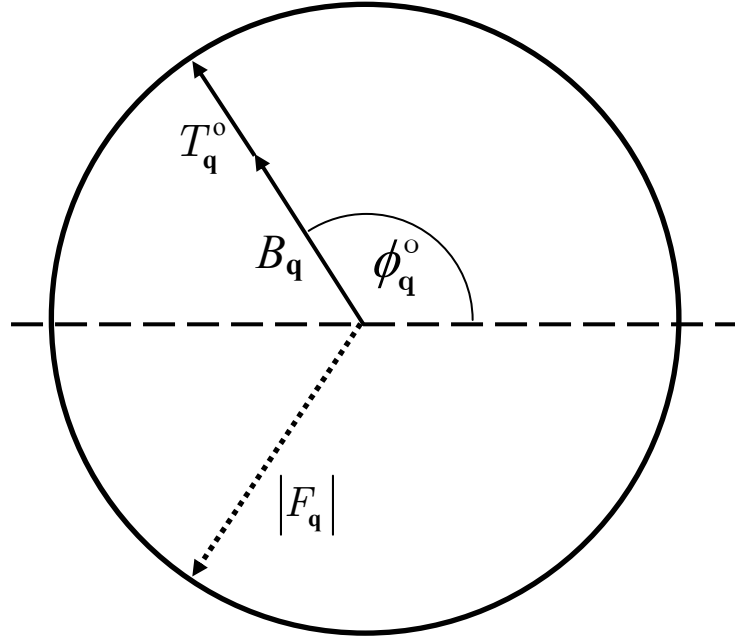


Figure 3.2 An amplitude-phase diagram showing a known complex bulk amplitude, $B_{\mathbf{q}}$, and the known modulus of the experimental amplitude which must lie somewhere on the circle shown. An initial estimate of the phases $\phi_{\mathbf{q}}$ then allows the formation of the reciprocal space target function $T_{\mathbf{q}}^{\circ}$.

This can be ensured by choosing

$$\lambda \ll 1/u_{\max}^{n-1}, \quad (3.27)$$

where u_{\max}^{n-1} is the maximum value of the distribution $\{u_i^{n-1}\}$. Thus (3.22) may be replaced

by the *explicit* recursion relation

$$u_i^n = u_i^{n-1} \exp\{-\lambda(u_i^{n-1} - t_i^{n-1})\} \quad (3.28)$$

so long as λ is chosen to satisfy (3.27).

The target function (3.21) has the form expected of the surface electron density: it consists of the Fourier transform of the difference between the total diffracted amplitude from the surface and that from the bulk. The only unknowns are the phases $\{\phi_{\mathbf{q}}\}$ of the measured data. Regardless of the choice of phases, the target function is a surface electron density that is in perfect agreement with the experimentally measured

amplitudes. An initial estimate of the target function $\{t_i^o\}$ requires initial estimates of the phases $\{\phi_q^o\}$. Figure 3.2 shows, in the complex plane, how this is done. The experimental amplitude are restricted to lie somewhere on the circle and the known bulk amplitude is represented by the vector labeled B_q . Following the prescription of the unweighted difference Fourier method of Cochran [Coc51] an adequate estimate of the initial phase is the argument of the amplitude from a surface represented by a truncated bulk structure. That is we take

$$\phi_q^o = \arg(B_q). \quad (3.29)$$

In Figure 3.2 this is shown by the fact that the initial reciprocal space target function T_q^o points in the same direction as the bulk amplitude. As for $\{u_i^o\}$, following Collins [Co82], we take this to be same as $\{t_i^o\}$ except that, to ensure positivity, we replace all values of the distribution which are less than 1/100th of the maximum value t_{max} (including all unphysical negative values) by $t_{max}/100$. Substitution of these distributions in the RHS of (3.28) enables the evaluation of the next estimate $\{u_i^1\}$ of the surface electron distribution. Values of the phases $\{\phi_q^n\}$ for $n > 0$ are estimated by eq.(3.19).

The equations (3.19), (3.21) and (3.28) represent a set of recursion relations. After the initial assignment of the phases, as described above, the algorithm then proceeds in a clockwise manner around the flow chart of Figure 3.3. The reciprocal space target function is formed with the current set of phases applied to the experimental amplitudes. This is represented, for iteration n , in the phase space diagram above the box containing the definition of the reciprocal space target function T_q^n in Figure 3.3. A Fourier transform yields the real-space target function $\{t_i\}$, which, in turn, is used to produce the next estimate of the electron distribution $\{u_i\}$, continuing around Figure 3.3

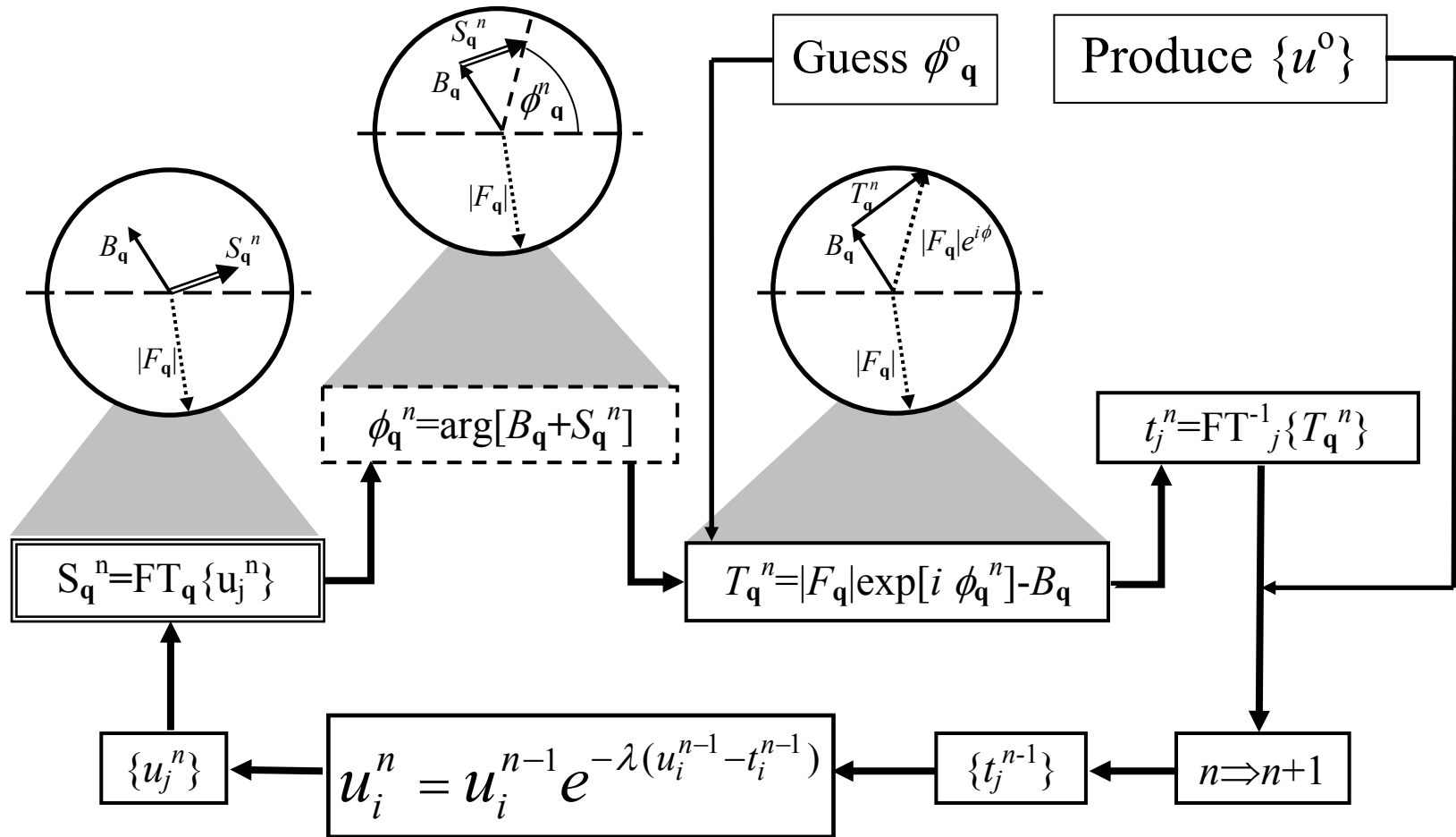


Figure 3.3 A flow chart of the MEM algorithm that operates in both real and reciprocal space. The initial guess of the phases is inserted into the expression for the reciprocal space target function. In the first iteration the initial electron density $\{u^0\}$ is obtained from $\{t^0\}$. The phase space diagrams above some boxes show the function of the operation in the complex plane.

clockwise. In the case of the first iteration, the initial distribution $\{u_i^o\}$ is also initialized as described above. An inverse Fourier transform then returns a improved estimate of the surface structure factor S_q , also shown in a phase space diagram above its definition in Figure 3.3 as the double line vector. The new estimate of phases $\{\phi_q\}$ is then obtained through the argument of the known bulk structure factor added to the new estimate of the surface structure factor. In terms of its repeated oscillation between real and reciprocal space, real space on the bottom of Figure 3.3 and reciprocal space on the top, this procedure also has something in common with the Gerchberg-Saxton algorithm [GS71], which is also used for recovering phases from a real-space amplitude distribution. In reciprocal space the total diffracted amplitudes are kept at their experimentally determined values. In real space the electron distribution is confined to its estimated physical bounds, through what is known as a support constraint. We too apply a support constraint in real space to the electron density at every iteration. In our case the support constraint only need be applied when the distribution $\{u_i\}$ is initialized, for once a voxel takes on an electron density of zero it will remain zero. The only other operation performed every iteration of Figure 3.3 is the normalization of the surface electron density distribution to the suspected number of electrons in the surface unit cell. We have found that the accuracy of this estimate is not a terribly critical factor in the ability of the algorithm to converge to the correct solution, though it is best that the estimate be larger than the actual number if it is not known exactly. The algorithm is iterated until convergence, which occurs when the current estimate of the surface electron density $\{u_i^n\}$ is “identical” to the target function $\{t_i^n\}$. In practice an R -factor of the form

$$R = \frac{1}{N} \sum_{\mathbf{q} \in Data} \frac{|I_{\mathbf{q}}^{Calc} - I_{\mathbf{q}}^{Exp}|}{I_{\mathbf{q}}^{Exp}} \quad (3.30)$$

is also monitored as a function of iteration number, where N is the total number of data points. When the graph of R vs. n is seen to approach a constant it is assumed that the algorithm has converged. The form of the iterative equation (3.28) guarantees convergence. In voxels where the density estimate u_i is higher than t_i the equation reduces the density. Just the opposite occurs where the estimate is lower than the current target.

This algorithm has been used to improve the resolution of a pre-existing electron density map of a protein beyond that obtainable from the measured data [Co82]. A similar exponential modeling scheme is used by Bricogne [Br84,Br88,Br91] and Gilmore[Gi96] as part of an iterative process in which a knowledge of phases of low resolution structure factors is extended to those of higher resolution shells. Given the reciprocal nature of the two spaces in which this algorithm operates; the resolution, or grid spacing on which the electron density is calculated, is determined by the maximum momentum transfer \mathbf{q} for which there is data. The concept of “super resolution”, often encountered in discussions of maximum entropy methods, is a process by which amplitudes and/or phases are synthesized by the algorithm at values of \mathbf{q} greater in magnitude than those previously obtained through experiment or other refinement techniques [Co82,Br84,Br88,Br91,Gi96]. To implement this concept in our algorithm we have to allow the algorithm to estimate both the phase and amplitude of unmeasured reflections. The algorithm accomplishes this through the nonlinear nature of the exponential iterative equation. The fact that it is nonlinear means that it changes the density distribution during an iteration in such a way as to add amplitudes to reciprocal space at values of \mathbf{q} greater than that for which data was measured. The fact that the

exponential iterative equation was derived through the constrained maximization of the entropy of the electron density distribution sought, lends some validity of the amplitudes it generates. Since in reciprocal space there are no constraints that can be imposed on these unmeasured amplitudes, they are effectively just left at the values obtained, until the next iteration through real space. An example showing the agreement between the synthesized amplitudes of the algorithm and the known amplitudes from simulation is presented at the end of the next chapter.

The overall smoothness of the electron density finally recovered is almost certainly due to the use of super resolution, as will be obvious in examples to follow. The higher order reflections that are created by the algorithm will help suppress the formation of “Gibbs Ears” in real space due to the sudden end of the data. The algorithm can self-impose something of a window function, as is often encountered in Fourier analysis of finite signals, to the data.

Chapter 4: Results From Simulated SXR D data

The algorithm described in the previous chapter has been applied to realistically simulated SXR D data from a number of test structures. Our adaptation of the ROD code by Vlieg was used for the simulation of the data [Vl00]. The tests were done on three-dimensional data sets simulated in what is believed to be an experimentally attainable range in reciprocal space. In the two cases presented the structures were previously determined from conventional analysis of diffraction data.

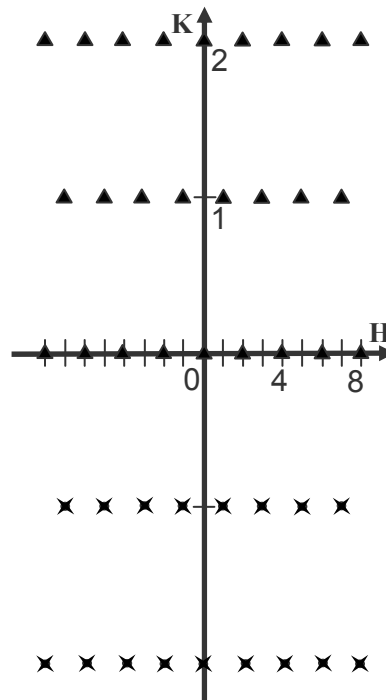


Fig 4.1 The diffraction pattern of the Cu(104) surface. The diagram indicates all of the CTR's used in the calculation. Those represented by four point stars are obtained through pm symmetrization of the rods represented by triangles.

Our first example is the O/Cu(104) surface whose structure has been determined by a conventional surface x-ray diffraction analysis [Wa99]. A slice through reciprocal space parallel to the surface will intersect these CTRs at the set of points characterized by the H and K Miller indices shown in Figure 4.1. The centered (1x1) surface unit cell

restricts the combination of H and K Miller indices specifying a CTR to those with even values of $(H+K)$. This general rule for centered unit cells can be seen from a two dimensional analysis of Figure 4.2. The two, inequivalent, atoms in this 2D unit cell are at $(0,0)$ and $(\frac{1}{2},\frac{1}{2})$. From eq (2.3) the bulk structure factor, as a function of Miller indices H and K will have the form

$$\begin{aligned} B_{H,K} &= f_b(H, K)(e^{2\pi i(H\cdot 0+K\cdot 0)} + e^{2\pi i(H\cdot \frac{1}{2}+K\cdot \frac{1}{2})}) \\ &= f_b(H, K)(1 + e^{\pi i(H+K)}) \end{aligned} \quad (4.1)$$

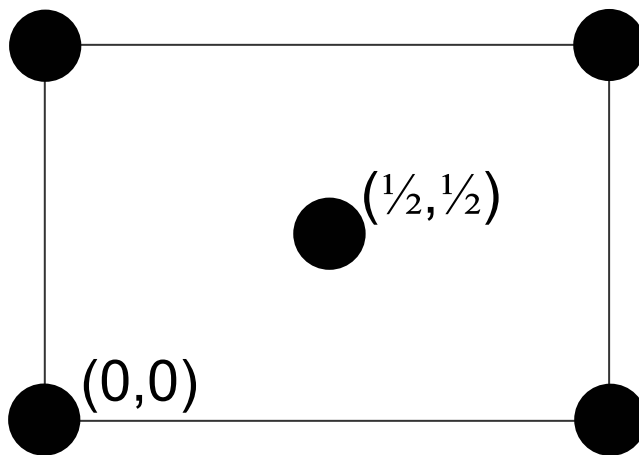


Figure 4.2 The geometry of a two dimensional centered unit cell. The coordinates are given in fractions of the unit cell vectors.

where we have once again assumed identical atoms, no Debye or absorption corrections and $L=0$ for simplicity. From eq. (4.1) it is obvious that the centered unit cell will have zero amplitude unless $(H+K)$ is even, for if $H+K$ is odd the two terms in the summation will cancel. Since in a centered unit cell, every atom in every layer will have a centered counterpart, the same rule will apply to even a three dimensional unit cell. Furthermore, due to the mirror planes perpendicular to the surface, in the case of Cu(104), and parallel to the H axis, it is necessary to measure only intensities of the rods with positive values of K , as shown as triangles in Figure 4.1 as triangles. For the purposes of our test we simulated the intensities of just those 26 of these inequivalent CTRs shown in Figure 4.1

7

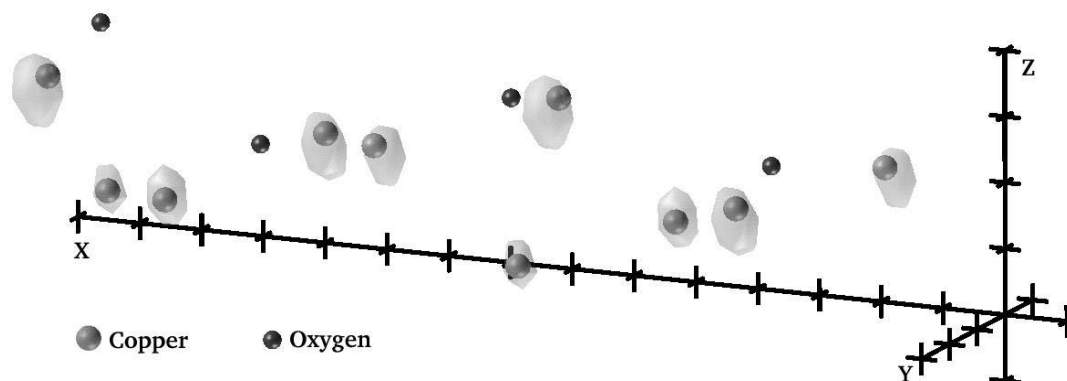


Figure 4.3 The initial electron density distribution obtained by applying the phases of the bulk unit cell to the data from O/Cu(104)-1x1.

for positive values of the Miller index L varying from 0 to 6.39 in intervals of 0.639. The combination of the mirror symmetry and Friedel's Law, ($F_{\mathbf{q}} = F_{\mathbf{q}^*}$), allowed us to deduce the intensities of all other CTRs shown in Figure 4.1 for both positive and negative L . The additional data required of our algorithm are of course calculated values of the amplitudes and phases of the corresponding structure factors of the assumed unreconstructed bulk structure of Cu(104). The same computer codes were used to calculate these amplitudes. In real space the electron density was confined, through a support constraint, to a height of five angstroms above the bulk termination. The algorithm was allowed to generate higher resolution amplitudes in reciprocal space given by $H_{max}=32$, $K_{max}=8$ and $L_{max}=19.8$, four times that of the maxima of data along H and K and about three times greater along L . The overall resolution of the electron densities shown in the figures is then about $\Delta x=0.23\text{\AA}$, $\Delta y=0.22\text{\AA}$ and $\Delta z=0.37\text{\AA}$.

Figure 4.3 shows a perspective view of surfaces of constant electron density (an

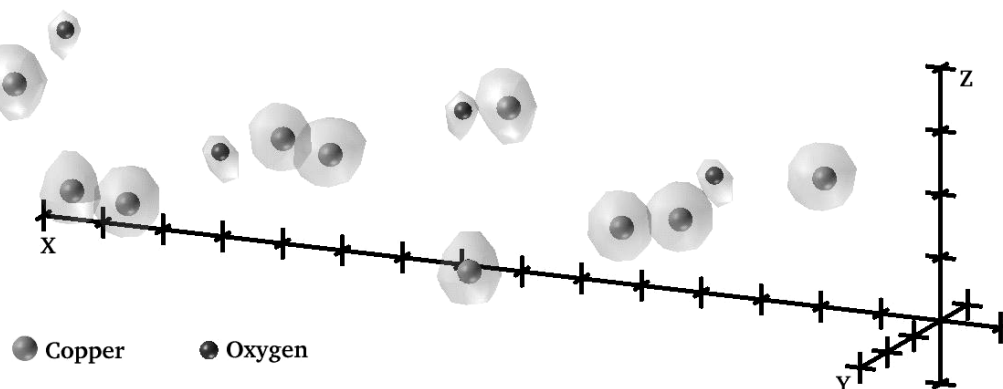


Figure 4.4 The final electron density distribution recovered for O/Cu(104)-1x1. The isosurface shown is at a level of .25 (where the maximum density is 2.0).

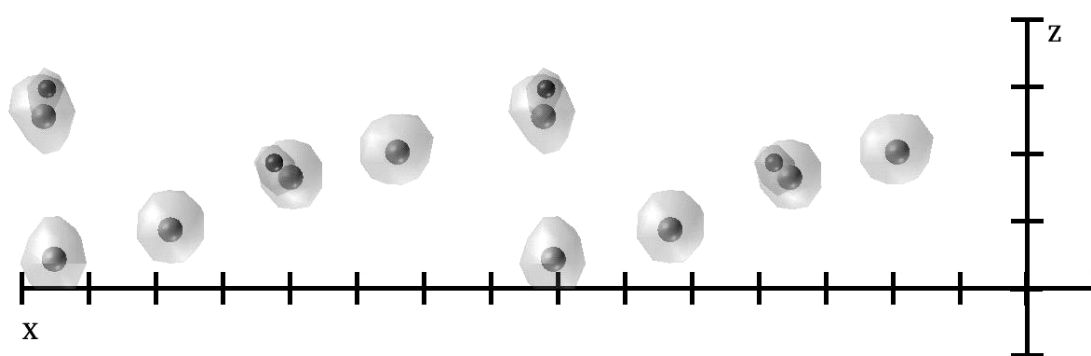


Figure 4.5 Side view of the final O/Cu(104)-1x1 surface electron density distribution.

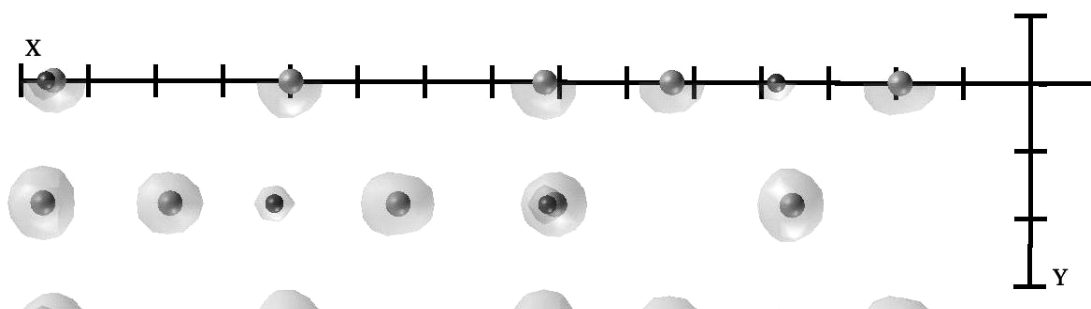


Figure 4.6 Top view of the final O/Cu(104)-1x1 surface electron density distribution.

isosurface) of the initial estimate $\{u_i^o\}$ of the distribution sought. This distribution is the so-called *difference Fourier* estimate. It is obtained, as specified in eq. (3.29), by applying phases from the bulk to the experimental amplitudes. The larger light-colored spheres represent the assumed positions of the surface Cu atoms, while the smaller dark spheres indicate the positions of

the adsorbate O atoms in the model of the surface used to create the simulated SXRD intensities. The initial electron density appears to be peaked around the Cu atoms with little indication of the O atoms. This is expected given that the Cu atoms in the surface

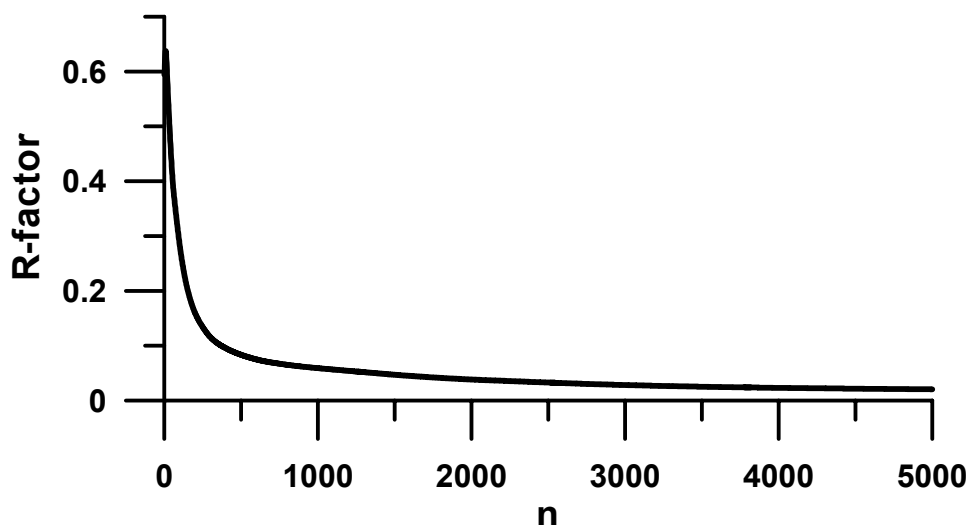


Figure 4.7 R-factor versus iteration number for recovery of O/Cu(104) surface density.

unit cell are displaced only slightly from their bulk positions and the initial phase estimate was from the known bulk.

Figure 4.4 shows the surface electron distribution after about 5000 iterations of eq (3.28), with λ set equal to $1/u_{max}$ at each iteration. Not only does the electron density around the O atoms now show up, but also that around the Cu substrate atoms appears more accurately centered around their true atom positions. The isosurfaces in figure 4.4 is at a level of 0.25; the maximum value of the electron density in the recovered distribution is about 2.0. The highest isosurface level at which non-atomic features (noise) appear is 0.05 and the algorithm was stopped at an R -factor of 0.059. Figure 4.7 shows the R -factor as a function of iteration number. It is seen to decrease rapidly at first and then slowly approach a minimum. After about the first 500 iterations the algorithm has essentially found the correct structure. The remainder of the iterations are reducing the

noise level and perhaps centering in on the atomic positions more exactly. Figures 4.5 and 4.6 show side and top views of the final electron distribution.

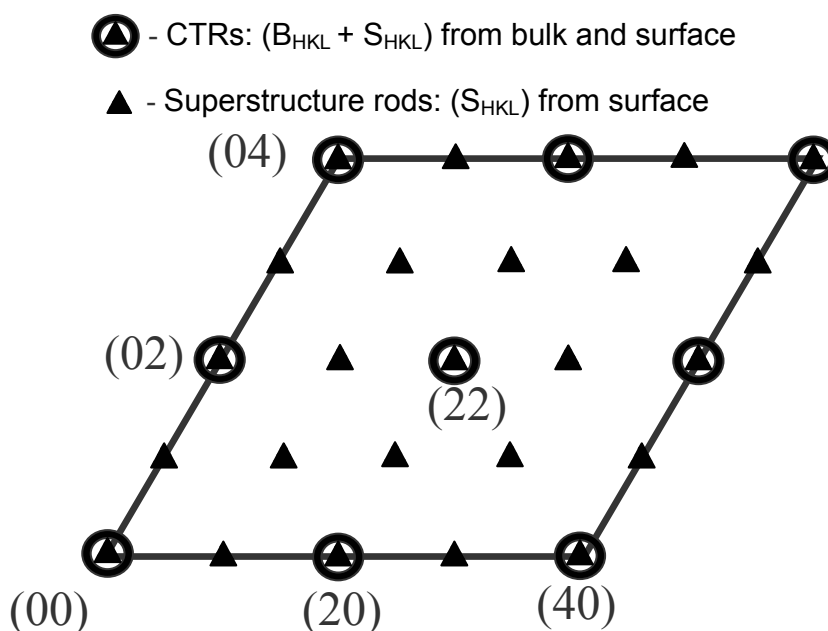


Figure 4.8 The asymmetric unit of the diffraction pattern from GaAs(111)-2x2. The full data set is obtained through the p3m1 symmetry of the surface.

A potentially tougher test is the recovery of the electron density of the outermost two double layers of the GaAs(111)-(2x2) surface. A conventional LEED analysis [To84] has established that this surface reconstructs into the so-called vacancy buckling structure, in which there is not only a large relaxation and reconstruction of the outermost bilayer, but there is also a vacancy formed in this layer at the corners of a (2x2) surface unit cell. Figure 4.8 shows a similar cut through reciprocal space parallel to the surface which now intersects both the CTRs, indexed by even values of the H and K Miller indices, and the superstructure rods characterized by odd values of either index. Recall that the superstructure intensities arise purely from the surface unit cell. Diffraction data from rods with values of $|H|, |K| \leq 4$ were used in this calculation. Figure 4.8 illustrates the asymmetric unit of diffraction intensities that were used in the recovery of the electron

density, combining the p3m1 symmetry of the surface with Friedel's law, all intensities from $H=-4$ to $H=4$ and $K=-4$ to $K=4$ as well as $L=-3.76$ to $+3.76$ with a ΔL of 0.47

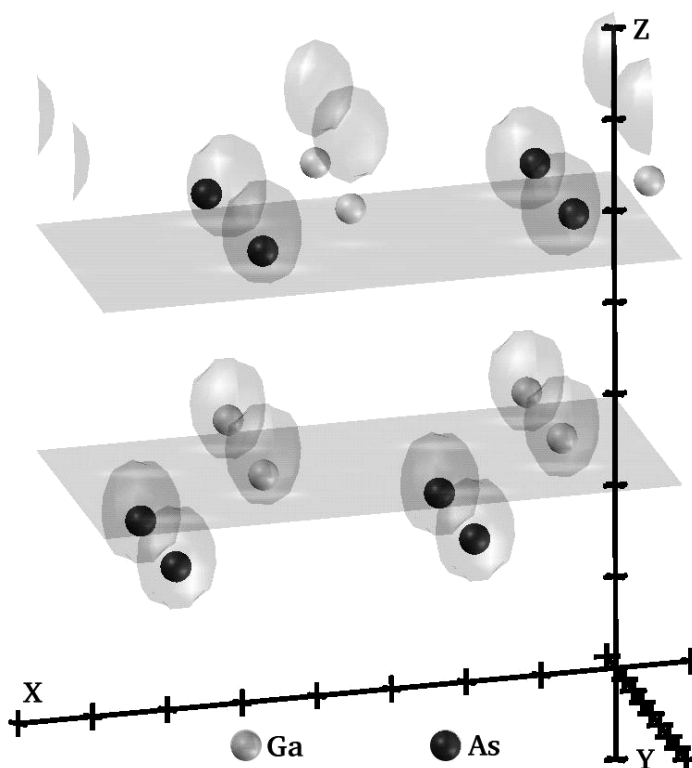


Figure 4.9 The initial surface electron density distribution used to begin recovery of the GaAs(111)-2x2 surface structure. Only CTRs are included with an initial phase estimate from the known bulk.

were given to the algorithm in this example, as well as the complex amplitudes from the bulk unit cell of GaAs(111). Only the CTRs may be initially assigned phases with reference to the bulk phases. Our strategy for dealing with this case is to begin by allowing the algorithm to operate on just the CTR data. The resulting surface electron density distribution will have a (1x1) periodicity that is the average of the density of each of the (1x1) quadrants of the true (2x2) periodicity. The starting distribution $\{u_i^0\}$ of the outermost two double layers of a (2x2) surface unit cell calculated from the initial assignment of the phases of the bulk to $\{\phi_q\}$ (followed by truncation of the negative values of $\{t_i^0\}$ as described previously) is shown in perspective in Figure 4.9.

The small spheres in Figures 4.9 through 4.11 mark the positions of the surface atoms in the model used to simulate the data, with the lighter-colored ones representing

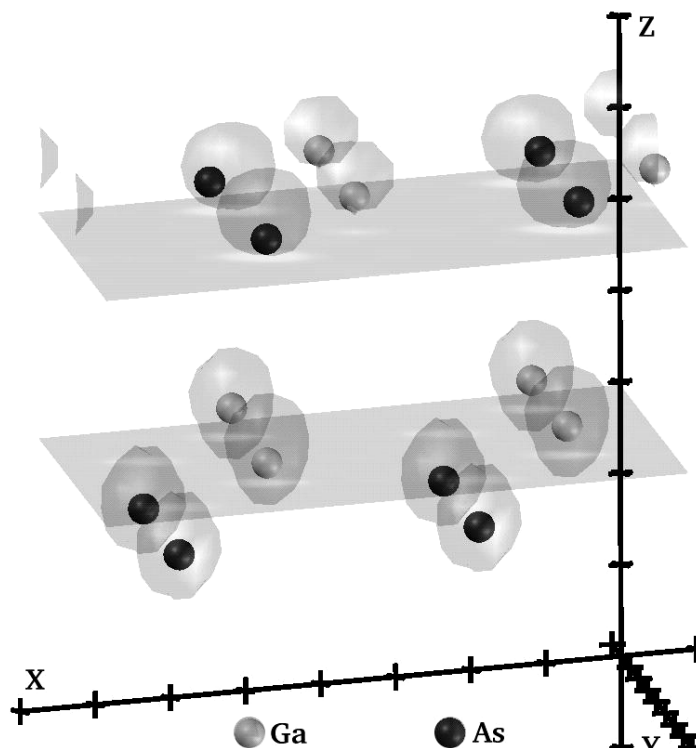


Figure 4.10 The 1×1 averaged surface electron density distribution of GaAs(111)- 2×2 . The isosurface shown is at a level of 0.12.

Ga atoms and the darker ones the As. One feature of the vacancy buckling model is that although the spacing of the lower double layer remains at approximately its bulk value, the uppermost double layer relaxes so as to make the two components of that double layer almost co-planar. This relaxation is recovered after 500 iterations of eq. (3.28) with just the CTR data. The distribution illustrated in Figure 4.10 shows almost co-planar isosurfaces associated with the Ga and As atoms in the outermost double layer, although naturally the (1×1) periodicity of the average structure remains.

The recovery of the true (2×2) periodicity of the surface requires the inclusion of data from the superstructure rods. This is accomplished by allowing the Fourier

summation for the target function (3.21) to include the amplitudes from the superstructure rods as well as the CTRs. The initial phases of these additional amplitudes

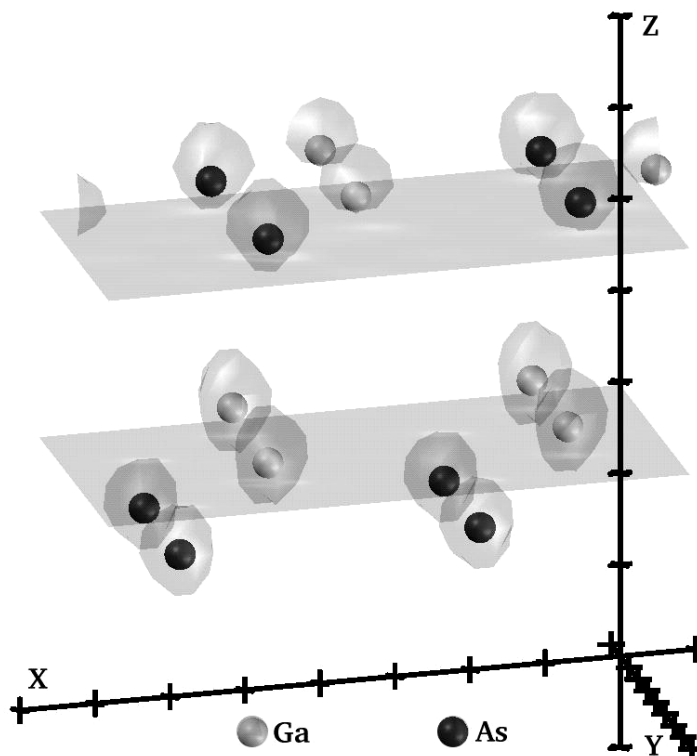


Figure 4.11 The final electron density distribution obtained for GaAs(111)-2x2. Shown at an isosurface level of 0.12 where the maximum density value is 7.77.

are set to zero, though algorithms immediately makes a more reasonable estimate during the first iteration after their inclusion. The resulting surface electron distribution after about 2500 further iterations of (3.28) is shown in 4.11. As in the case of O/Cu(104) the value of λ used in the iterative equation is $1/u_{max}$ at each iteration. These isosurfaces are seen to accurately pinpoint the locations of all atoms in the vacancy buckling model. It correctly reproduces the (2x2) 2D periodicity and shows the vacancy at the corners of the (2x2) unit cell along the z axis. As can be seen in the *R*-factor graph of Figure 4.12, after the initial phasing of the CTRs upon inclusion of the superstructure rods the *R*-factor takes a sharp jump, due to the relatively poor initial phases for the

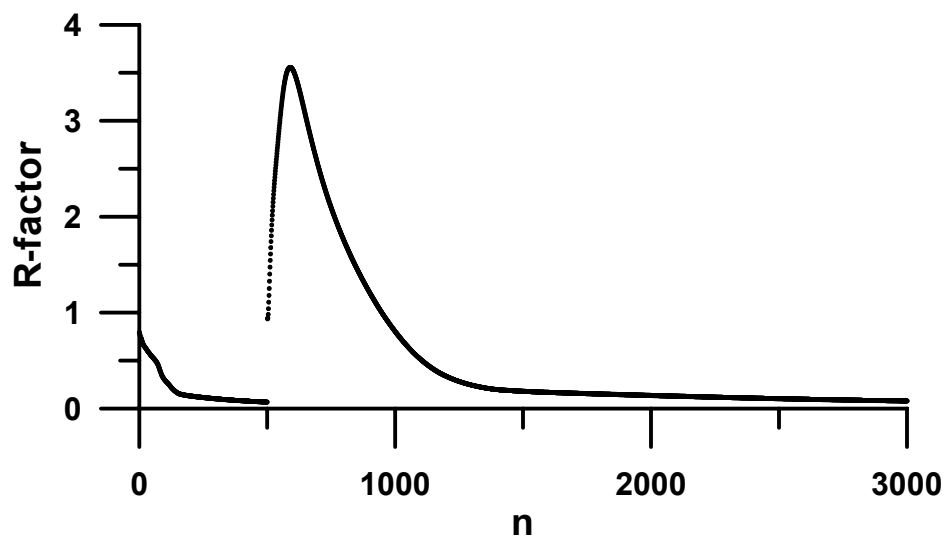


Figure 4.12 The R -factor as a function of iteration for the recovery of GaAs(111)-2x2. The algorithm was stopped at 500 iterations and the superstructure amplitudes were then included in the recovery.

superstructure spots, and then continues to climb for about 100 more iterations. This clearly shows the ability of the MEM to avoid stagnation in local minima of the R -factor. The R -factor when the algorithm was finally halted was about 0.08.

As in the O/Cu(104) case, the algorithm was allowed to extend the amplitudes

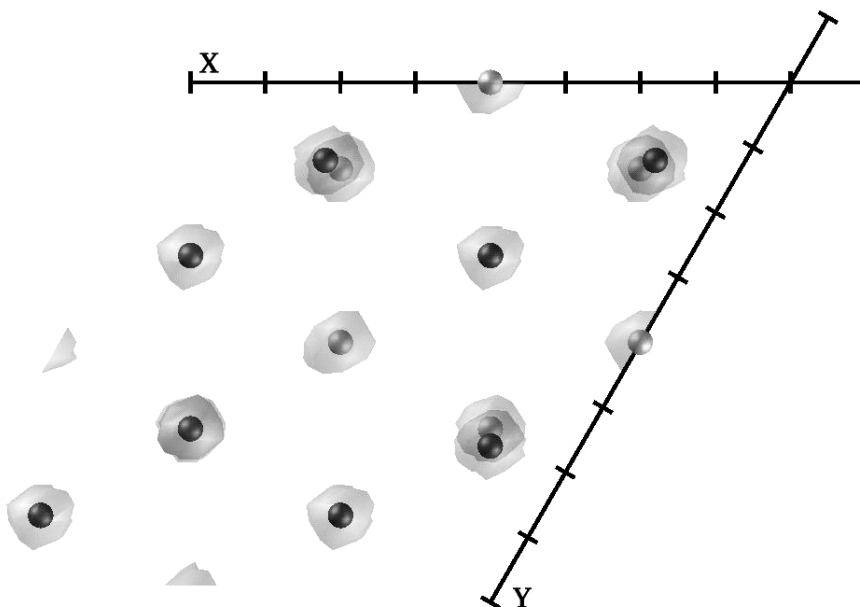


Figure 4.13 Top view of the density recovered for GaAs(111)-2x2.

into higher resolution reflections. In this case the maximum value of H and K allowed is 16 and the maximum L allowed is 19.8. The resulting resolution of the densities shown in the figures is about 0.25\AA in all directions. The noise level in the density recovered in the end is effectively zero, meaning that at no observable isosurface level could noise be seen. Figure 4.13 is a top view of the electron density recovered in the end. It shows relatively good centering of the isosurface on the atomic coordinates used in the simulation of the data. The perspective views show that perhaps the vertical locations could be better determined, but again, this method is only meant to give a starting point for a conventional refinement.

To illustrate the “super-resolution” aspect of the MEM algorithm let us return to the O/Cu(104) example given above. Since we are working with simulated data there is no reason the exact surface structure factors, outside of the data set given to the algorithm, cannot be compared to those synthesized in the course of recovering the surface electron density distribution. The graphs in Figure 4.14 show the modulus squared of the surface structure factors $|S_{\mathbf{q}}|^2$, both from the program used to simulate the actual data (dashed lines) and the values extracted from the MEM program at the end of the O/Cu(104) structure determination (solid lines). These graphs allow a comparison between the amplitudes synthesized by the algorithm to the actual values of these amplitudes. Figures 4.14 (a) and (b) illustrate the ability of the algorithm to extend the data to values higher than $L=6.39$, which was the maximum value of L in the data set, for a given value of H and K . Up to $L=6.39$ in these graphs the agreement is obviously very good. The only reason they are not identical is probably due to the fact that the real space target function, whose reciprocal space counterpart would be in perfect agreement up to

$L=6.39$, probably still contains some negative values for which the electron density distribution $\{u\}$ would have very small values. Beyond $L=6.39$ in figures 4.14 (a) and (b) the agreement is better in (b), although in both the variation is very similar implying that the Fourier transforms of the complex amplitudes are probably very similar.

Figure 4.14 (c) and (d) are the same as (a) and (b) except these are for values of H and K for which there was no data what so ever given to the algorithm. Figure 4.14(d) is obviously the better of the two, showing oscillations very similar to the actual values.

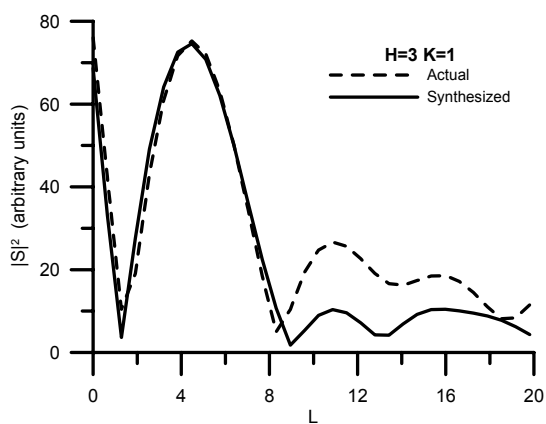


Figure 4.14(a)

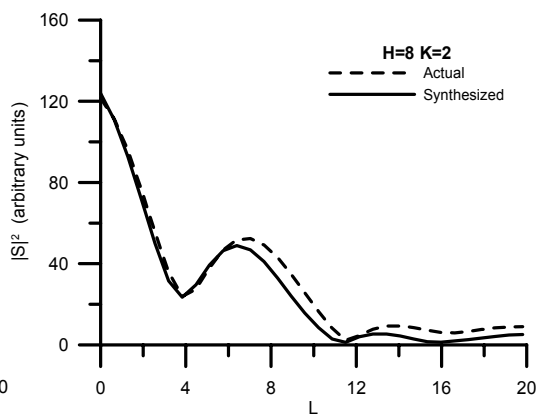


Figure 4.14(b)

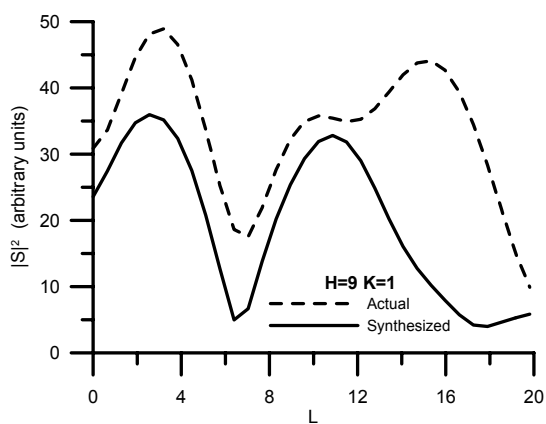


Figure 4.14(c)

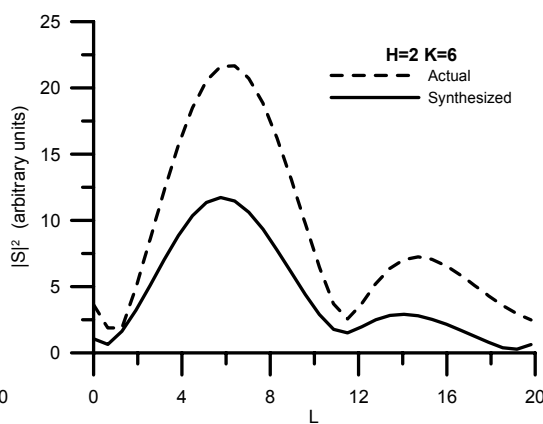


Figure 4.14(d)

Figure 4.14 Super-resolution for O/Cu(104). The dashed lines are the actual simulated values of $|S_q|^2$ for the given rod from O/Cu(104). The Solid lines represent that created by the MEM algorithm. Figures (a) and (b) above show the ability of the MEM algorithm to extend the data to higher values of L than that contained in rods included in the data set. The data in these rods ended at $L=6.39$. Figures (c) and (d) allow comparison of rods which were completely synthesized by the MEM algorithm.

Figure 4.14(c) is an example of the worst the synthesis seems to get. These four examples are a good representation of the algorithm's extension of the data to higher resolution reflection. They also seem to consistently show that the algorithm's synthesized amplitudes are lower in magnitude than the actual magnitudes. This could be evidence of the window function effect mentioned in Chapter 3. If the amplitudes do not come to a sharp end in reciprocal space it will tend to make the electron density smoother in real space. Since it takes high frequency sines and cosines in real space to produce a sharp edge in reciprocal space these high frequency components in real space will tend to make the electron density distribution appear spiky and unphysical.

Chapter 5: Mixed Domain surfaces and Results from SXR

Often the surface of a crystal can contain multiple domains in which the surface is covered by the same surface unit cell which has been rotated or mirrored. Depending on the size of the domains with respect to the coherence length of the x-rays, the diffracted beams from each domain can add either coherently or incoherently. When the domain size is smaller than the coherence length of the x-rays the overlapping beams will add coherently meaning that they each have a distinct phase and will interfere. In the case of larger domains the relative phases of the beams overlapping from each domain are essentially randomized and the intensities are added [Ro92],[VI00].

In the first of these two cases, coherent addition of the domains, the algorithm presented in the preceding chapters can be used unmodified, as long as the result is interpreted correctly. Here the measured intensities are of the form

$$I_{\mathbf{q}} = \left| f (B_{\mathbf{q}} + S_{\mathbf{q}}) + (1-f)(B_{\mathbf{q}'} + S_{\mathbf{q}'}) \right|^2, \quad (5.1)$$

where f is the fraction of the surface occupied by one domain and $(1-f)$ the fraction occupied by the other [Ro92],[VI00]. $B_{\mathbf{q}}$ and $S_{\mathbf{q}}$ are the structure factors from the bulk and surface unit cells as defined in (2.3) and (2.5). The structure factors denoted by momentum transfer \mathbf{q}' are the contribution to diffraction spot \mathbf{q} from the rotated domain.

The vector \mathbf{q}' is given by

$$\mathbf{q}' = \mathbf{A}^{-1} \mathbf{q}, \quad (5.2)$$

where the matrix \mathbf{A} is the real space transformation that relates the two domains. In practice there could be more than two symmetrically related domains, in this text we will

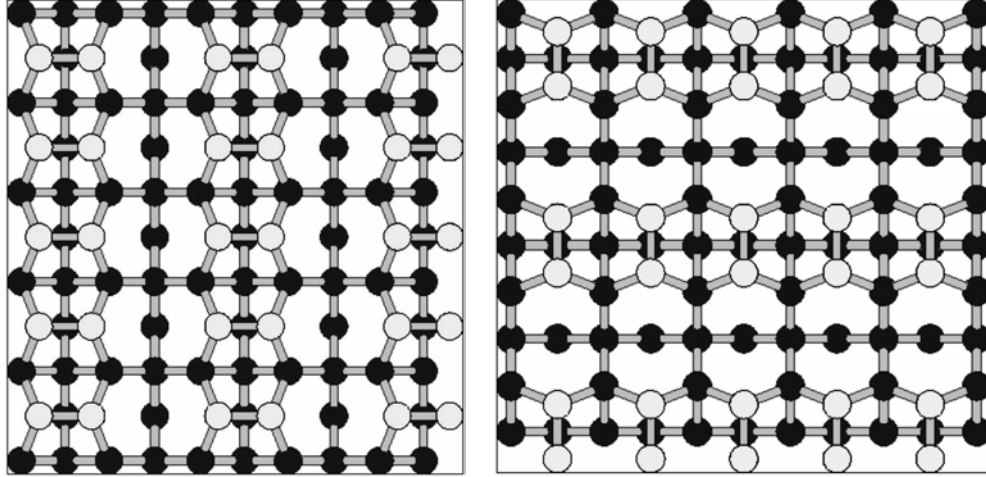


Figure 5.1 An illustration of a surface with two domains which are rotated with respect to each other. The example shown here is Ge(001)-2x1 with 90° rotated domains. The dimer layer has been highlighted, by making the circles lighter, for the demonstration found later.

focus on the case of two domains. There is no obvious reason that the algorithm developed should not be applicable to more than two such domains.

The key to applying the algorithm to intensities of this type is to identify the electron density distribution that has been termed the target function. In the case of a single domain it took the form of (3.21). The target function for the case of coherently added domains is

$$t_i^{(n-1)} = \frac{1}{N} \sum_{\mathbf{q}} \left\{ 2 |F_{\mathbf{q}}^{\text{exp}}| \exp(i\phi_{\mathbf{q}}^{(n-1)}) - B_{\mathbf{q}} - B_{\mathbf{q}'} \right\} \exp(-i\mathbf{q} \cdot \mathbf{r}_i) \quad (5.3)$$

where we have taken $f=1/2$ for the remainder of this description, assuming equal occupancy of each domain, and $|F_{\mathbf{q}}^{\text{Exp}}| = \sqrt{I_{\mathbf{q}}^{\text{Exp}}}$. To identify this as the target function, (5.1) is simply solved for $S_{\mathbf{q}} + S_{\mathbf{q}'}$. Inserting this target function into the algorithm, the recovered surface electron density will be the superposition of the two surface domains.

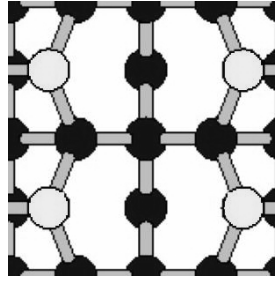


Figure 5.2 The (2x2) unit cell used in the simulation of data from two domains. The lightly filled circles, forming the dimmers, are the Ge composing in the surface unit cell.

This idea has been tested using simulated experimental intensities from a hypothetical parallel dimer reconstruction of a Ge(001)-(2x1) surface as illustrated in Figure 5.1. For the purpose of this test we assumed all atoms below the dimer layer to be in their bulk positions. Also, as a computational convenience, we take the surface unit cell to be two neighboring (2x1) unit cells to form a 2x2 repeat unit, shown in Figure 5.2. Two domains were included in the simulated intensities, rotated ninety degrees with respect to each other. The unit cell of each domain contains four dimer atoms, seen in Figure 5.2. The superposed electron density recovered by the algorithm will contain eight atoms in total.

The (2x2) “mesh” is used is to simplify the interpretation of the Miller indices with respect to each domain. If the true (2x1) unit cell were used it would complicate the combining of intensities from the two domains. An example in the case of Ge(001) would be the $H=2, K=0$ intensities from one domain would have to be incoherently averaged with the $H=0, K=1$ intensities from the other domain. The use of the (2x2) mesh allows the $H=0, K=2$ spot from the second domain to be averaged with the $H=2, K=0$ spot of the first.

A slice through the diffraction rods in reciprocal space is shown in Figure 5.3. At even values of the Miller indices H and K , the CTRs in this case, the intensity is

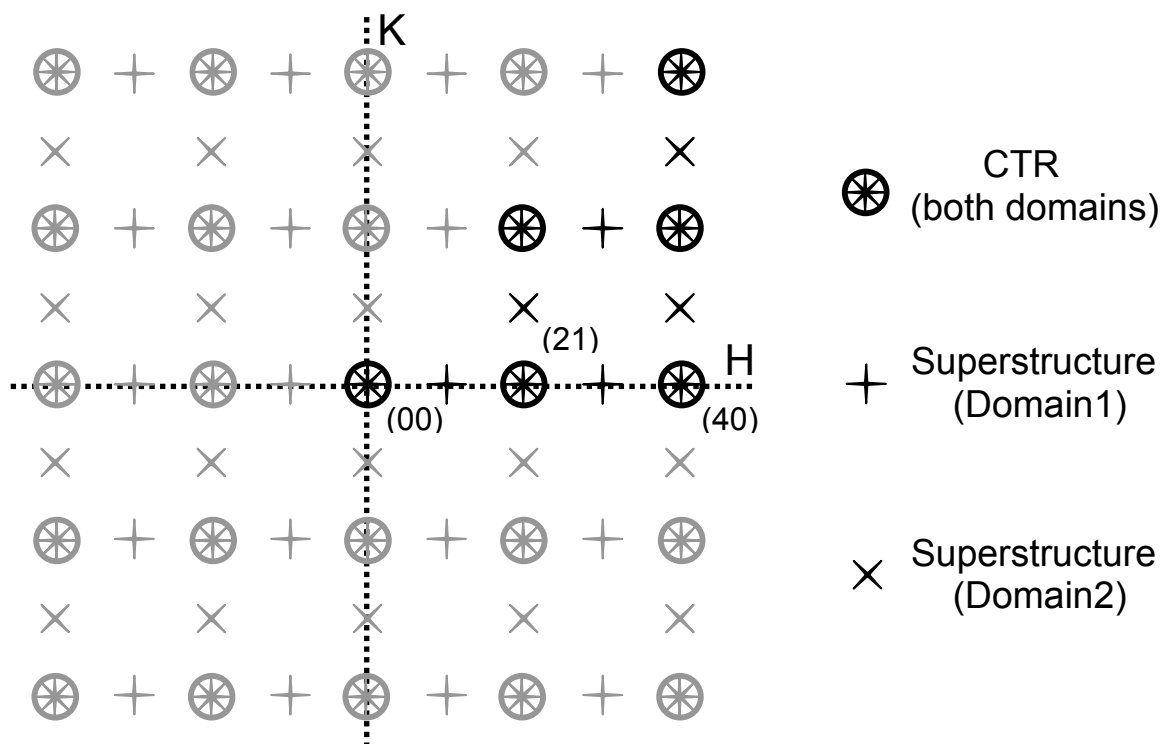


Figure 5.3 Diffraction pattern from Ge(001)-2x1 in a 2x2 mesh with two domains at right angles to each other. The black symbols are the asymmetric unit of data given to the algorithm; the gray symbols are obtained through symmetry.

composed of contributions from both domains. In case of the superstructure rods, odd values of H or K , only one of the two domains will contribute. The black symbols in Figure 5.3 represent all of the diffraction rods given to the algorithm, the gray symbols are obtained through both the $p2mm$ symmetry of the unit cell and the rotational symmetry of the domains.

The program is executed in much the same way as it was for the GaAs(111)-(2x2) example given previously. The algorithm is started with just the phases of the bulk applied to the CTRs, the inverse Fourier transform of this, with the negatives truncated, is shown in Figure 5.4. First only the CTRs are allowed to be phased by the algorithm, maintaining the superstructure rods at zero. The result of the initial phasing is the (1x1) averaged electron density in the four quadrants of the (2x2) unit cell. This intermediate

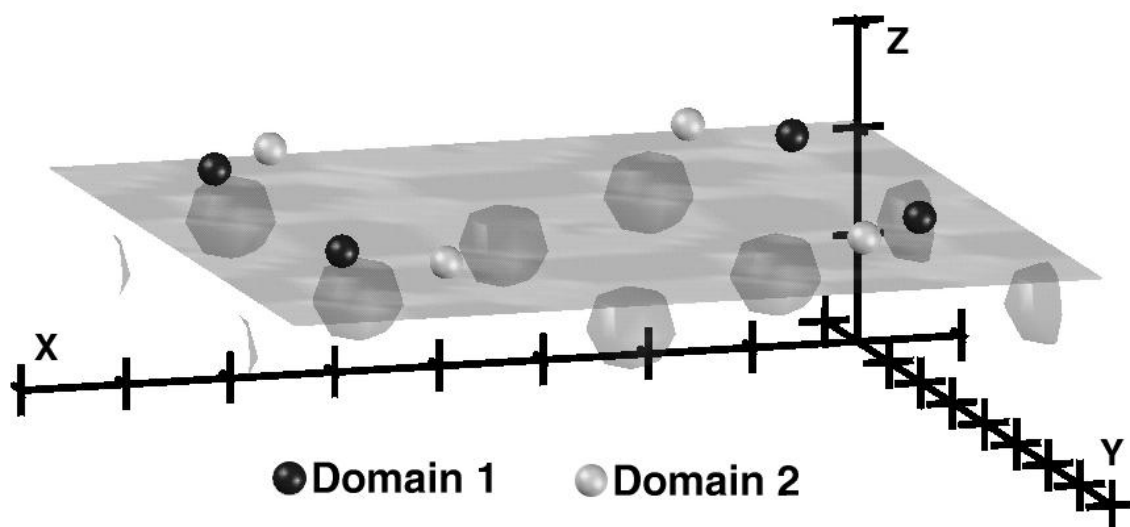


Figure 5.4 The initial surface electron density distribution, for recovery of our hypothetical Ge(001)-2x1 two domain structure, created through application of phases from the bulk unit cell to the experimental CTRs. The dark spheres represent the atomic position used in the model, the lighter are the symmetrically equivalent second domain.

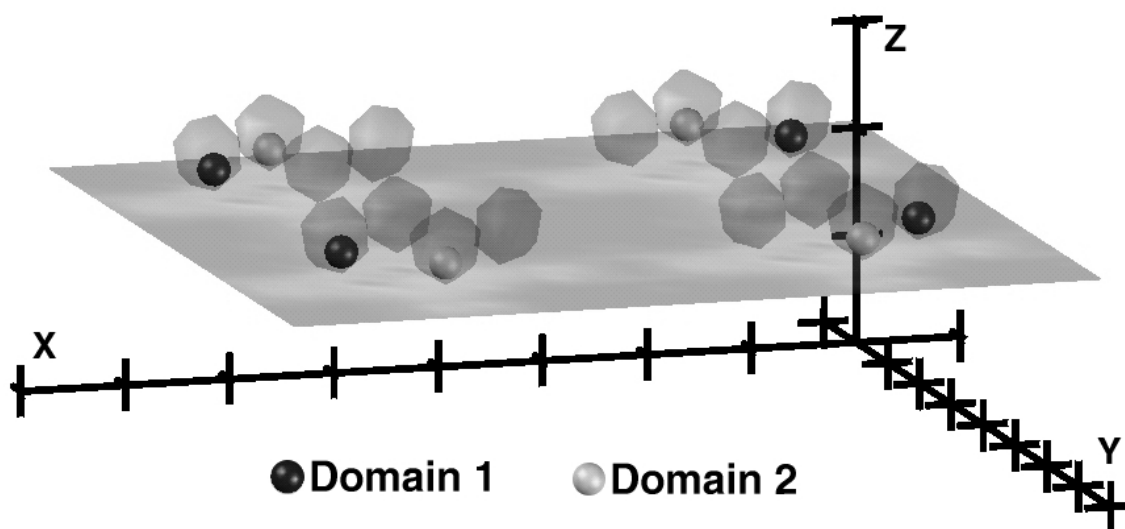


Figure 5.5 The averaged 1x1 surface electron density distribution of our model for Ge(001)-2x1 with two domains for which the scattered amplitudes have been added coherently.

result is shown in Figure 5.5 after 250 iterations. The true (2x2) periodicity is recovered when the algorithm is then allowed to include the superstructure rods, with initial phases set to zero, and is also allowed to continue to refine the CTRs. The final (2x2) unit cell with superposed domains is shown in Figure 5.6 after an additional 750 iterations.

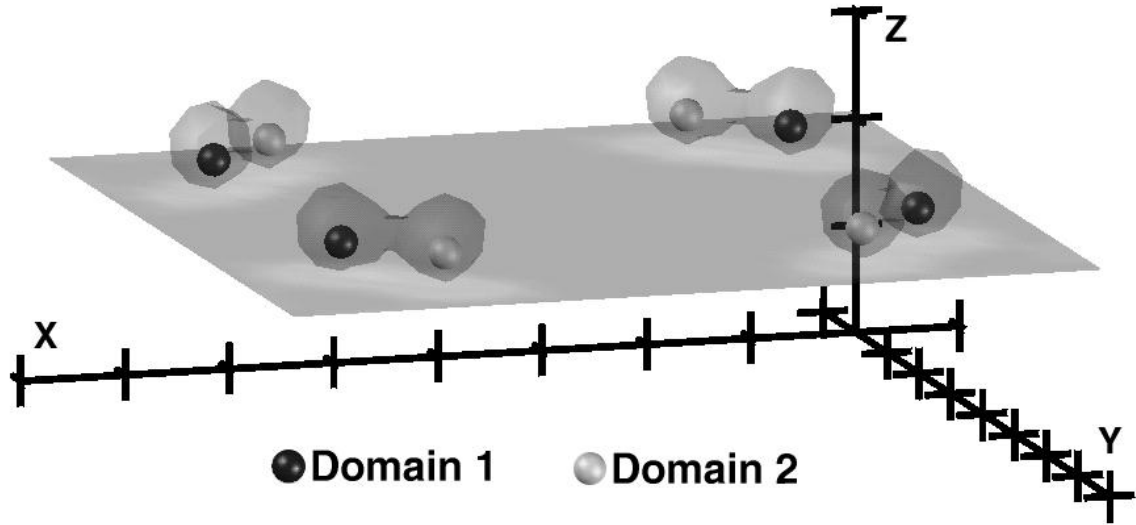


Figure 5.6 The final electron density distribution recovered upon inclusion of the superstructure rods from Ge(001)-2x1. A low isosurface level of 0.25 was chosen to make the density isosurface more obvious in the figure. The maximum density value is 3.98.

As in the single domain examples the algorithm has been allowed to extend the resolution to greater values of q than for which data was provided. In this case H_{max} and K_{max} are set to 16 while L_{max} is 9.585. These values are four times greater than the maxima of data in both H and K and about two and a half times greater than the maximum value of L in the data at 3.83. Along the profile of the rods this corresponds to seven values with a spacing of 0.639. As a result of the higher resolution components the final electron density seen in Figure 5.6 has a resolution of 0.25\AA along the X and Y axis and about 0.3\AA along the Z axis. The noise level in these densities, as in the case of densities recovered for single domains, is very low. In Figure 5.6 the maximum observable noise is .04 where the maximum density is about 3.98. The support constraint, the height above which the density is fixed to be zero, is set to 4\AA for this test.

Similar to the example of a single domain of GaAs(111)-2x2 the R -factor, in figure 5.7, jumped suddenly upon inclusion of the superstructure amplitudes at 250

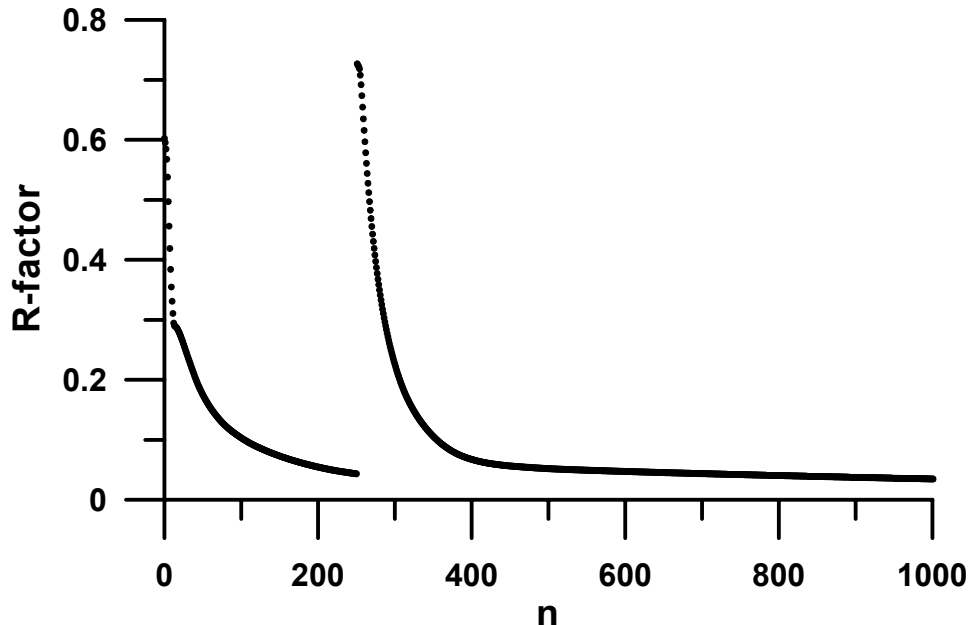


Figure 5.7 The R-factor as a function of iteration number during the recovery of Ge(001)-2x1 from coherently added scattering amplitudes from two domains. The minimum reached at the 1000th iteration is .035.

iterations. The fact that the initial phases of these reflections are taken to be zero makes this result unsurprising. The R -factor is then observed to sharply decrease almost immediately in the end reaching a value of 0.035.

The measured intensities from a pair of incoherently added domains take the form

$$I_{\mathbf{q}} = f |B_{\mathbf{q}} + S_{\mathbf{q}}|^2 + (1 - f) |B_{\mathbf{q}'} + S_{\mathbf{q}'}|^2 \quad (5.4)$$

where, just as in the coherent addition case, the primed and unprimed \mathbf{q} are related through (5.2) [Ro92],[Vl00]. Again, for the remainder of this discussion we will assume $f=1/2$ and just two symmetrically related domains. In principle this method should work for the case of more than two incoherently averaged domains.

To identify the target function of our algorithm from this intensity, once again we solve eq. (5.4) for the structure factor of the surface unit cell as we did in the case of coherently averaged domains. The difference with the incoherent case is that we will isolate the surface structure factor from just one of the two domains and as a result

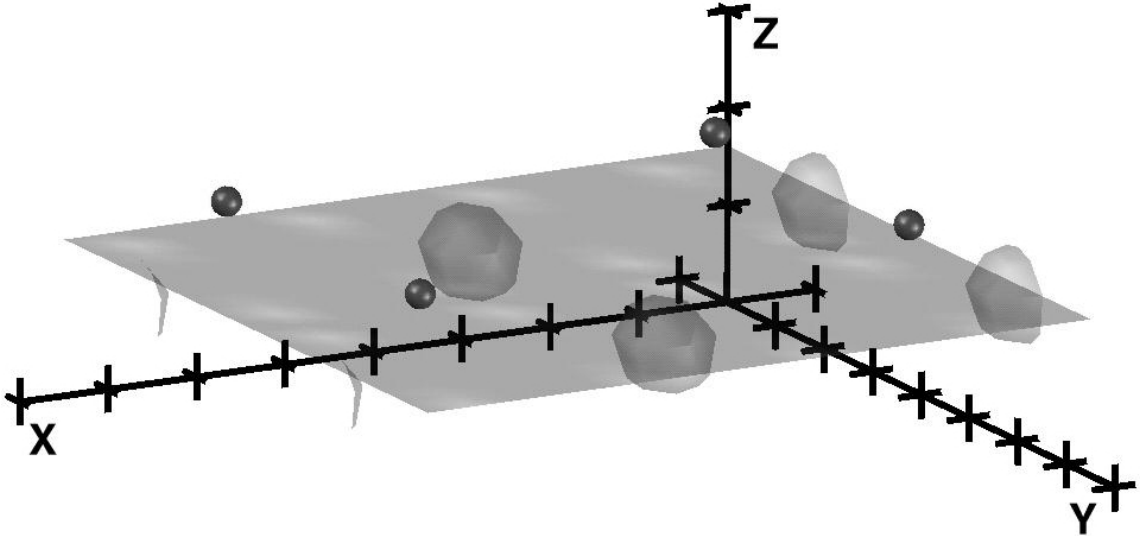


Figure 5.8 The initial surface electron density distribution used for the recovery of the structure Ge(001)-2x1 from incoherently averaged SXRD intensities of two domains.

recover the electron density from just that one domain, as opposed to a superposition of the two domains in the coherent case. Doing this gives the follow target function

$$t_i^{(n-1)} = \frac{1}{N} \sum_{\mathbf{q}} \left\{ \sqrt{2I_{\mathbf{q}}^{\text{exp}} - |B_{\mathbf{q}'} + S_{\mathbf{q}'}|^2} \exp(i\phi_{\mathbf{q}}^{(n-1)}) - B_{\mathbf{q}} \right\} \exp(-i\mathbf{q} \cdot \mathbf{r}_i) \quad (5.5)$$

which can now be inserted into the algorithm developed herein and iterated.

For the purpose of testing our algorithm in this application the same structure, Ge(001)-(2x1), was used in a simulation of SXRD intensities, following eq. (5.4), from two domains of equal proportions. The initial guess of the density, in this case, is just that of a truncated bulk unit cell and is shown in Figure 5.8. Given the form of the target function(5.5), an initial guess of phases is not enough. This is due to the fact that the intensities from the second domain, including the surface contribution, need to be subtracted from the total experimental intensities before an initial set of phases can be used to produce the initial target function.

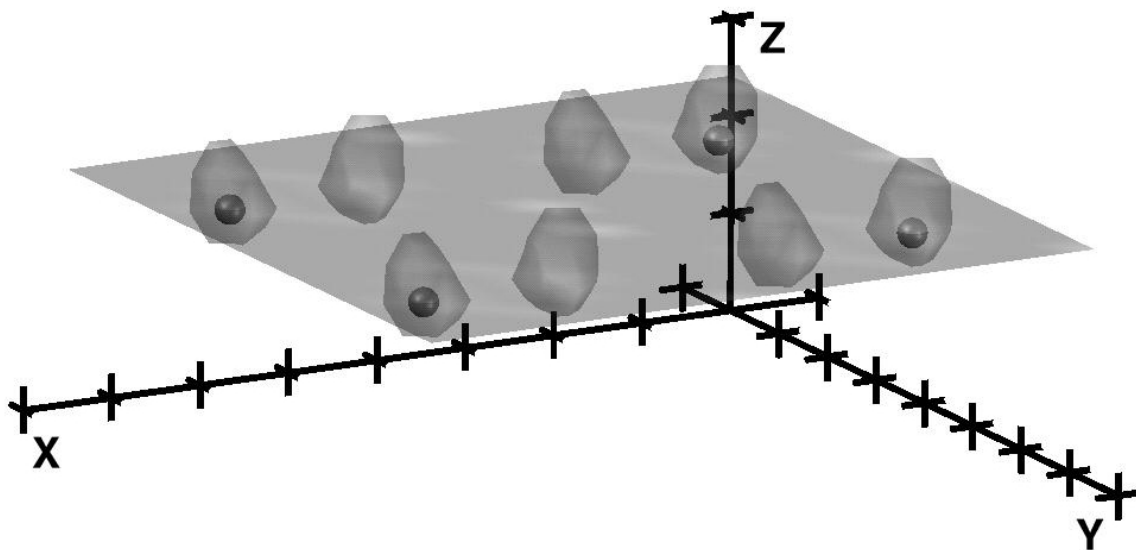


Figure 5.9 The averaged 1×1 surface electron density distribution of our model for Ge(001)- 2×1 with two domains for which the scattered amplitudes have been added incoherently. Shown at an isosurface level of 0.44 where the maximum density level is .98 at this intermediate stage.

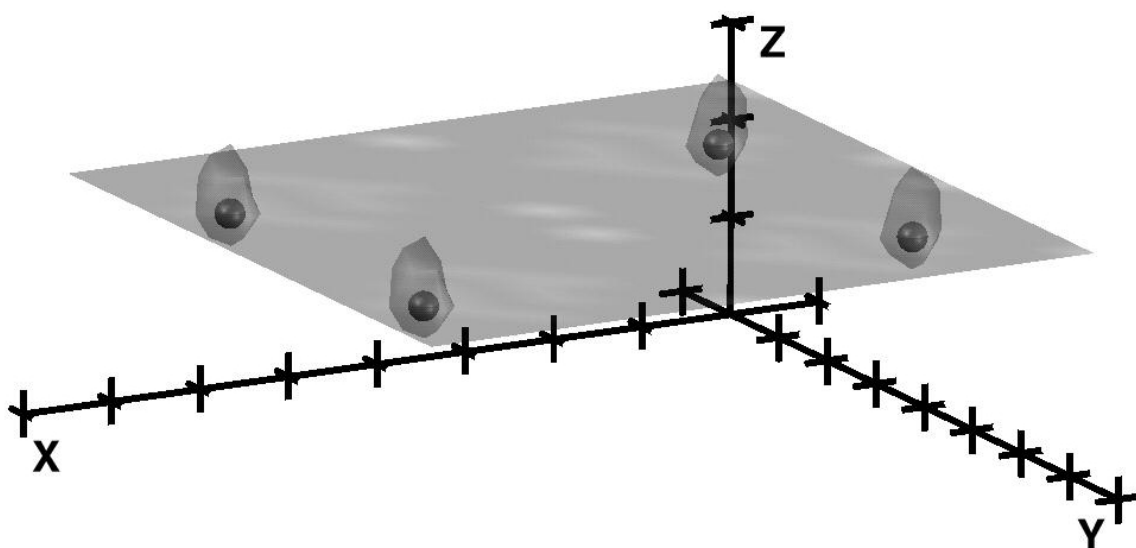


Figure 5.10 The final electron density distribution recovered from incoherently averaged domains upon inclusion of the superstructure rods from Ge(001)- 2×1 . Shown at an isosurface level of 0.9 where the maximum density value is 9.68.

As in the previous examples, the algorithm is first allowed to phase just the CTRs. The (1×1) averaged structure recovered during this stage is shown in Figure 5.9 after 500 iterations. Then the algorithm is allowed to phase both the CTRs and the superstructure rods until convergence. An isosurface of the electron density finally recovered is shown in Figure 5.10.

The diffraction pattern for incoherently added domains is identical, although the amplitudes are different, to that of the coherent case shown in Figure 5.3. The algorithm is given the same set of incoherently averaged diffraction rods shown in this figure recalculated for the new case. There are a few differences in the data sets however: in this case the value of δL along the rod profiles is 0.47 giving a maximum value of 3.76 in nine data points; as a result the resolution of the final electron density along the Z axis is 0.19\AA due to the maximum value of L accessible to the algorithm for extension of the data being 14.57. The resolution along the X and Y axis is the same as the coherent example, 0.25\AA .

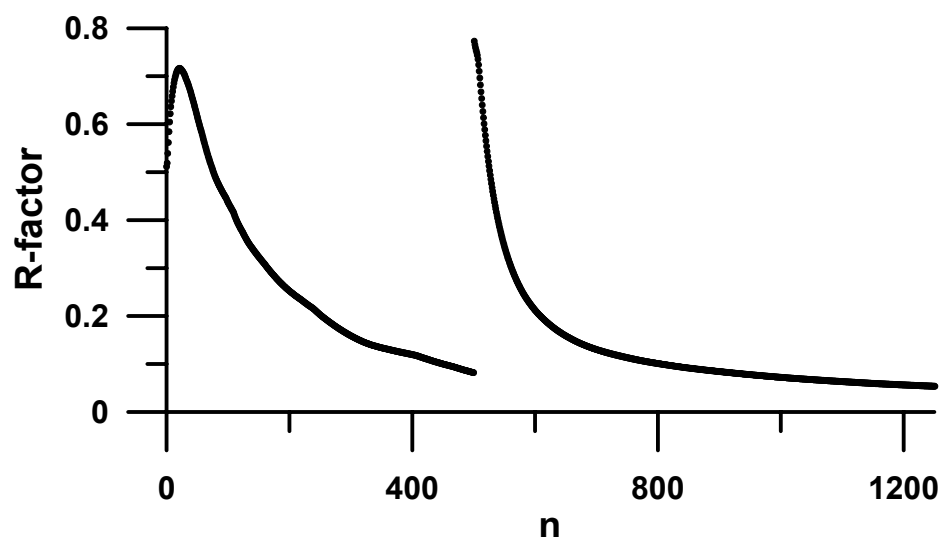


Figure 5.11 The R -factor as a function of iteration number during the recovery of Ge(001)-2x1 from incoherently added scattering amplitudes from two domains. The value at the 1250th iteration is 0.054.

The R -factor graph in figure 5.11 shows, once again, the ability of the MEM to avoid stagnation in local R -factor minima. In the initial phasing of the CTRs the R -factor is observed to rise sharply before beginning a downward trend. At 500 iterations the algorithm is then allowed to include the superstructure rods. As we have come to expect, the R -factor made a jump, given that superstructure rods outnumber the CTRs in the data

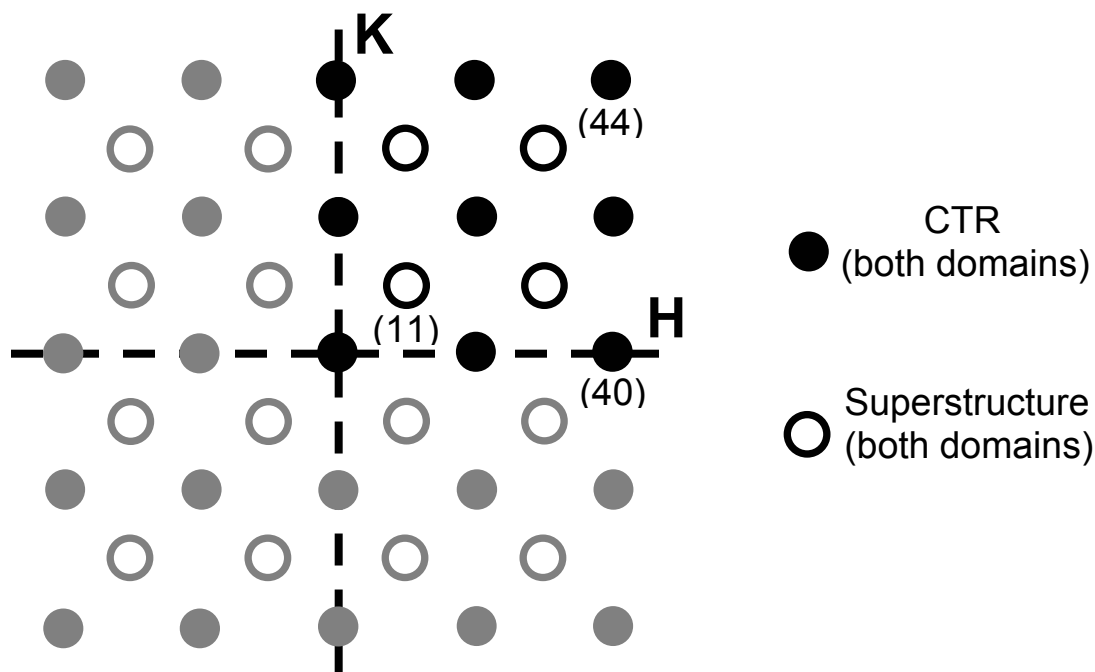


Figure 5.12 Diffraction pattern from $\text{TiO}_2(001)\text{-c}2\times 2$ with two domains mirrored with respect to one another. The black symbols are the asymmetric unit of data given to the algorithm; the gray symbols are obtained through symmetry.

set by 8 to 5, it is not surprising that it rose to a level greater than even the initial value for the CTRs. At 1250 iterations, when the algorithm was stopped, the R -factor had reached a value of about 0.054.

Another example of a structure that was recovered from simulated incoherently averaged intensities is a hypothetical model for $c(2\times 2)\text{-K/TiO}_2$. In this model the second, symmetrically related domain is a mirror about the Y axis of the first. This structure, unlike the $\text{Ge}(001)\text{-}2\times 1$ example has a surface unit cell with atoms at different heights, as well as a diffraction pattern in which both the CTRs and superstructure rods are incoherently averaged in contrast to the $\text{Ge}(001)$ model discussed earlier in which the superstructure spots arose from just one of the two domains. Figure 5.12 shows a slice through reciprocal space of the simulated data used in this example. The centered nature of this hypothetical model again restricts the intensity to even values of $H+K$. The initial

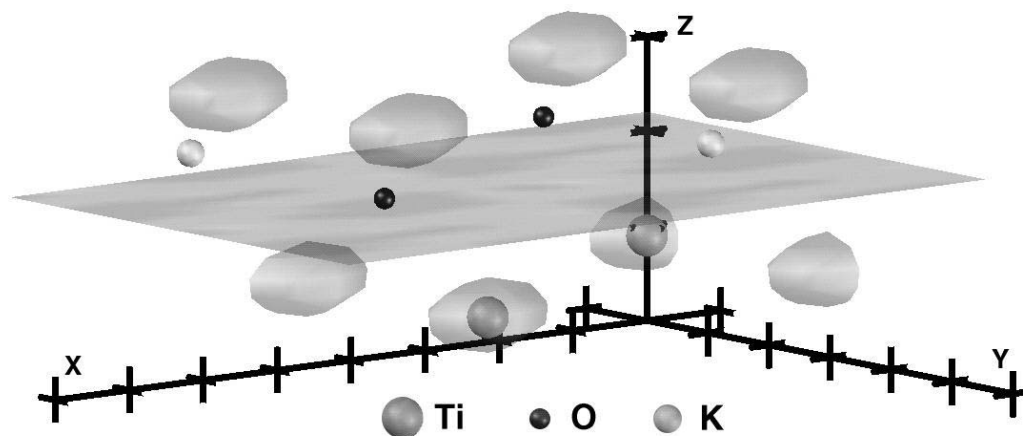


Figure 5.13 The initial electron density given to the algorithm for the recovery of K/TiO_2 from two incoherently averaged domains. Shown at an isosurface level .15 where the maximum is 0.45.

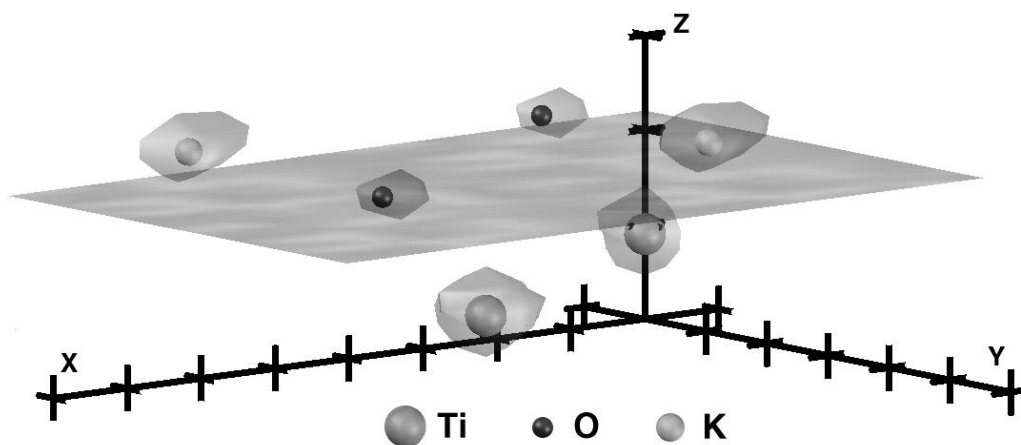


Figure 5.14 The final electron density distribution recovered from incoherently averaged intensities from two domains of a hypothetical $c(2 \times 2)\text{-K/TiO}_2$. Shown at an isosurface level of 0.35 where the maximum is 3.73.

guess at the density given to the program is shown in Figure 5.13, as usual it is of the truncated bulk unit cell within the support constraint maintained throughout the algorithms execution at about 4 Å. This time the algorithm was allowed to use both the CTR and superstructure data from the start. The recovered density is shown in Figure 5.14. In fact it was found that the oxygen atoms, which are relatively light in comparison to titanium and potassium, were not recovered if the CTRs were initially phased

separately. This is our first test structure for which the CTRs outnumber the superstructure rods in the data set used. It is possible that the ratio of CTRs to superstructure rods is a factor that can help determine if an initial phasing of the CTRs is necessary in application of this method to true experimental data from an unknown surface. The R -factor plot as a function of iteration number, Figure 5.15, shows the rather unsurprising rapid decline followed by a steady approach to a minimum of about 0.039.

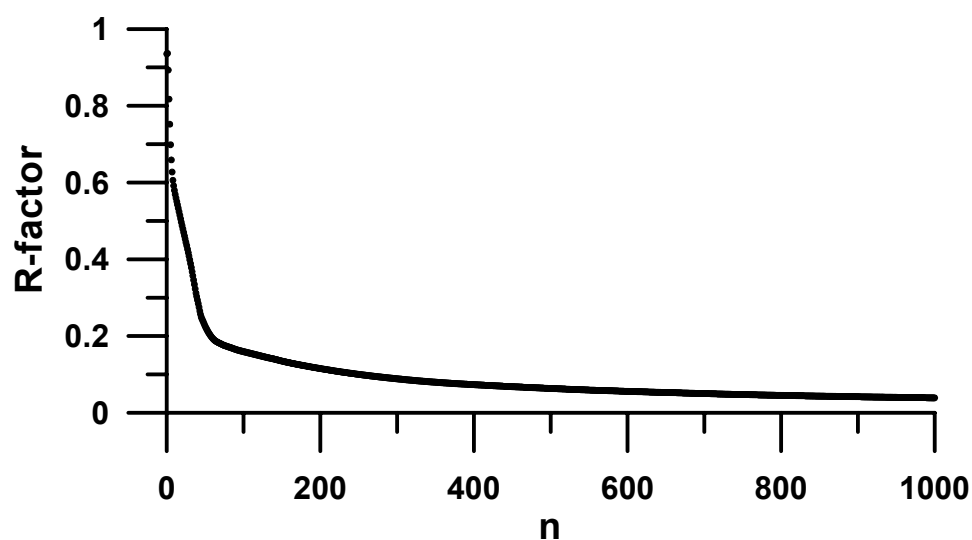


Figure 5.15 The R -factor, as a function of iteration number, for the recovery of a hypothetical model for K/TiO_2 in mirrored domains which have been incoherently averaged. The value at the 1000th iteration is 0.039.

Chapter 6: Extension of MEM to LEED

Another type of diffraction experiment which is sensitive to the structure of the surface is low energy electron diffraction (LEED) [3,26]. In a LEED experiment a beam of electrons is directed into the sample from a distant source and the intensities of elastically backscattered electrons, with different momentum transfers parallel to the surface, are monitored as a function of the incident electron energy. Due to the periodicity parallel to the surface, in analogy with the SXR D experiment described in chapter 2, the parallel momentum transfer vector must be a 2D reciprocal lattice vector of the surface, i.e.

$$\mathbf{q}_{\parallel} = \mathbf{g} = H\mathbf{a}^* + K\mathbf{b}^* . \quad (6.1)$$

Each diffraction data point may be specified by an index ε representing a combination of the diffracted beam parallel momentum transfer \mathbf{g} and electron energy E . The main difference between SXR D and LEED is that, due to the presence of strong multiple scattering of the electrons, there exists no simple Fourier transform relationship between any physical characteristic of the structure and the diffraction amplitudes. Nevertheless, by identifying an appropriate analogy to the Fourier transform of the amplitudes as well as analogies to the previous interpretation of the SXR D data, an adaptation of the maximum entropy theory developed above, for the case of SXR D, is able to determine the structure from LEED data. The following derivation is taken from the paper by R.J. Harder and D.K. Saldin 2002 *Holographic Surface Crystallography: Substrate as Reference* in M.A. Van Hove and W. Schattke (Eds.) *Solid State Photoemission and Electron Diffraction*, in press. [ME02].

The first analogy with SXRD is that, even in the case of strong multiple scattering, the dynamical (or multiple-scattering) structure factor may be written as the sum

$$F_{\varepsilon} = R_{\varepsilon} + S_{\varepsilon}, \quad (6.2)$$

where R_{ε} is the dynamical structure factor of the bulk crystal, which may be calculated exactly if the structure of the bulk is known. S_{ε} will then represent the effect of all multiple-scattering paths that include at least one scattering event in the surface unit cell. Secondly, in LEED, to a very good approximation it is possible to express S_{ε} in the form

$$S_{\varepsilon} = \sum_j p_j O_{\varepsilon j} \quad (6.3)$$

where $O_{\varepsilon j}$ represents a *renormalized scattering matrix* (in a plane-wave representation) of a primitive 2D test superlattice, which includes an atom at a position j with respect to the substrate. The term *renormalization* implies only multiple-scattering between that layer and the substrate is included in the calculation of this matrix. It may be regarded as a form of *elementary object wave* [Sz93], which may be calculated without knowledge of the surface unit cell structure. The quantity S_{ε} is thus regarded as a linear combination of calculable elementary object waves, with a set of real and non-negative expansion coefficients p_j . This representation of S_{ε} is an approximation that neglects multiple scattering between the sublattices represented by the quantities $O_{\varepsilon j}$. Even in the case of a CO molecule normally oriented on a surface, where the dominant forward scattering of the O would create a high expectation for another scattering from the C, this approximation appears to be sufficient as will be illustrated in the example given later. The important point is that writing the structure factor in the form

$$F_\varepsilon = R_\varepsilon + \sum_j p_j O_{\varepsilon j} \quad (6.4)$$

makes it formally similar to the corresponding expression

$$F_q^{calc} = B_q + \sum_j u_j \exp(i\mathbf{q}\cdot\mathbf{r}_j) \quad (6.5)$$

in surface x-ray diffraction. Thus the third analogy between LEED and SXRD is given by the similar roles of the distributions $\{p_j\}$ and $\{u_j\}$, which suggests that $\{p_j\}$ may be determined by a similar maximum entropy algorithm from experimental LEED intensities.

Accordingly, we define an entropy of the distribution $\{p_j\}$ by the expression

$$S[\{p_l^n\}] = -\sum_l p_l^n \ln(p_l^n / ep_l^{n-1}) \quad (6.6)$$

of the unknown distribution $\{p_l^n\}$ at iteration n , relative to the distribution $\{p_l^{n-1}\}$ at the previous iteration, and a functional

$$Q[\{p_l^n\}] = -\sum_l p_l^n \ln\left(\frac{p_l^n}{ep_l^{n-1}}\right) - \frac{\lambda'}{2} \sum_\varepsilon \frac{|S_\varepsilon^n - T_\varepsilon^{n-1}|^2}{\sigma_\varepsilon^2}. \quad (6.7)$$

in analogy with eq. (3.17) where the distribution $\{p_l^n\}$ substitutes for the electron density distribution $\{u_l^n\}$ at the n^{th} iteration,

$$S_\varepsilon^n = \sum_l p_l^n O_{\varepsilon l} \quad (6.8)$$

$$T_\varepsilon^{n-1} = |F_\varepsilon| \exp[i\phi_\varepsilon^{n-1}] - R_\varepsilon \quad (6.9)$$

and,

$$\phi_\varepsilon^{n-1} = \arg[R_\varepsilon + S_\varepsilon^{n-1}]. \quad (6.10)$$

The quantity σ_ε in eq. (6.7) is the estimated uncertainty in the measured structure factor amplitude $|F_\varepsilon|$, and λ is a Lagrange multiplier. Q may be maximized by requiring that

$$\frac{\partial Q}{\partial p_j^{(n)}} = 0 \quad \forall j. \quad (6.11)$$

The differentiation of the entropy term in eq. (6.7) is straightforward; that of the constraint term is carried out by writing $|S_\varepsilon^n - T_\varepsilon^{n-1}|^2$ as $\{S_\varepsilon^n - T_\varepsilon^{n-1}\}$ times its complex conjugate and noting that O_ε^n depends on p_j^n , but T_ε^{n-1} does not. After some algebra we obtain

$$\ln \left[\frac{p_j^n}{p_j^{n-1}} \right] = -\lambda \left\{ \mu_j^n - \tau_j^{n-1} \right\}, \quad (6.12)$$

where

$$\mu_j^n = \frac{1}{N} \sum_\varepsilon \text{Re} \left\{ S_\varepsilon^n O_{\varepsilon j}^* \right\} \quad (6.13)$$

and

$$\tau_j^n = \frac{1}{N} \sum_\varepsilon \text{Re} \left\{ T_\varepsilon^n O_{\varepsilon j}^* \right\}, \quad (6.14)$$

as well as $\lambda = \lambda' N / \langle \sigma_\varepsilon^2 \rangle$, where the individual variances σ_ε^2 are replaced by their mean value, we finally obtain

$$p_j^n = p_j^{n-1} \exp \left[-\lambda \left\{ \mu_j^n - \tau_j^{n-1} \right\} \right]. \quad (6.15)$$

Together with eqs. (6.10), (6.13) and (6.14), this constitutes an *implicit* relation for p_j^n in terms of $\{p_i^n\}$. It can be written as an *explicit* equation for p_j^n by substituting μ_j^{n-1} for μ_j^n on the RHS. By analogy with the x-ray case we would expect this to be valid if λ were

chosen small enough. From the x-ray analogy we conjecture that the condition on λ in the LEED case is

$$\lambda \ll 1/p_{\max}^{n-1} \quad (6.16)$$

where p_{\max}^{n-1} is the maximum value of the distribution $\{p_j^{n-1}\}$. Thus we argue that eq.

(6.15) may be replaced by the following *explicit* recursion relation:

$$p_j^n = p_j^{n-1} \exp\left[-\lambda \left\{ \mu_j^{n-1} - \tau_j^{n-1} \right\}\right] \quad (6.17)$$

so long as λ satisfies eq. (6.16).

We will now consider the form of R_e and O_{ej} used in an implementation of the algorithm. Firstly consider the scattering of a LEED electron from an ordered 2D test layer of the periodicity of the superlattice on top of a substrate. Assuming that the substrate is of a known structure, it is possible to calculate exactly its reflection matrix B^{++} in a plane wave basis. If the “in-out” scattering matrix of the test layer (in the same basis) is defined as M^{-+} , and the “in-in” matrix as M^{++} and the “out-out” matrix as M^{--} in the usual LEED notation, where the right superscript denotes the direction of incidence on the layer or substrate and the left superscript the direction of scattering (or transmission) of the wave, where + is into the solid and – is out of the solid. Exploiting the weakness of back-scattering processes compared to forward-scattering ones, the scattering paths involving the substrate and test overlayer may be ordered by the number of back-scattering processes involved. Obviously, since the minimum number of back-scatterings involving the overlayer is one, paths that involve more than one overlayer back-scattering can be neglected in our implementation. Also, exploiting the weakness of $\sim 90^\circ$ scattering of LEED electrons of normal incidence compared to either forward or

back scattered, we approximate the scattering matrices $M^{\pm\pm}$ by “kinematic” expressions [Pe74], that neglect multiple scattering within the test overlayer [Bi85].

Suppose the electron cloud associated with the surface extends to a height h above the uppermost atomic layer of the substrate, as illustrated in Figure 6.1. The propagation of electrons below this height must take into account both the refraction and adsorption associated with being inside the surface potential. It is thus convenient to define an origin O in this interface plane at height h with respect to which is measured the phases of all plane waves considered in our expressions for R and S . Define also an origin j of

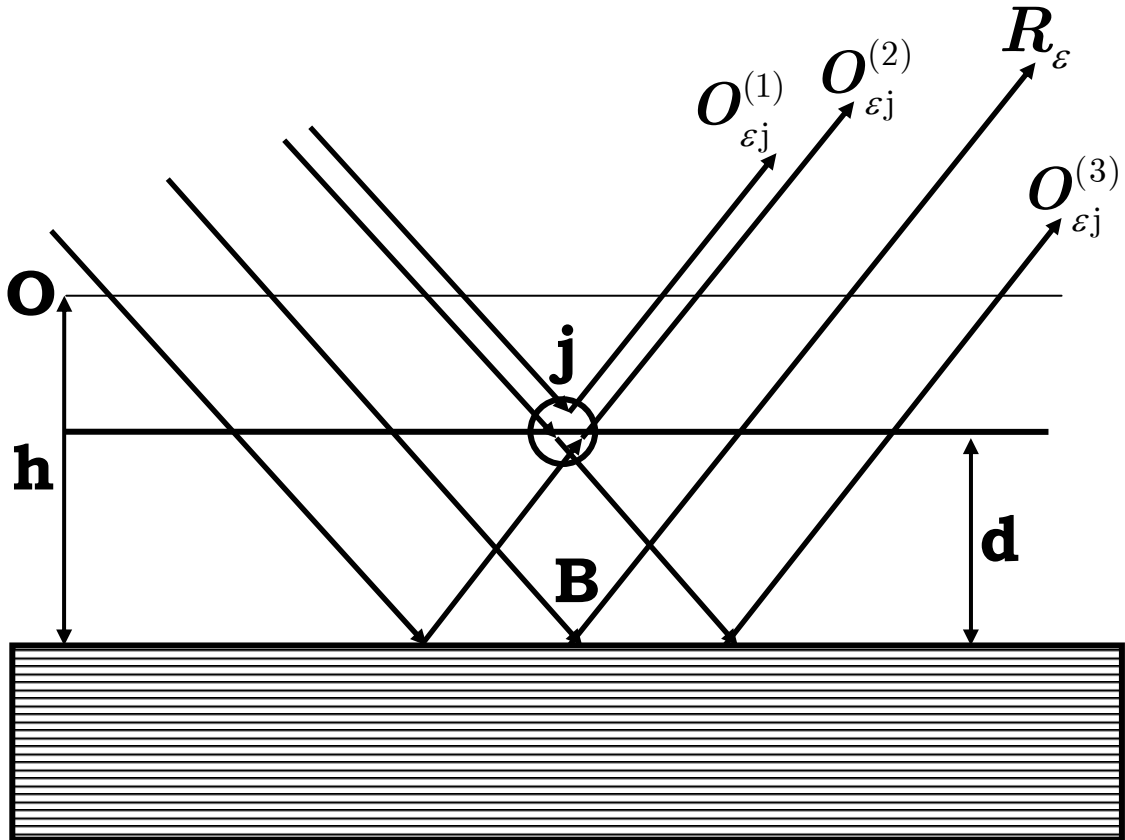


Figure 6.1 Representation of the electron propagation and scattering paths giving rise to the *reference wave* R_{ϵ} and the three dominant contributions $O_{\epsilon j}^{(1)}$, $O_{\epsilon j}^{(2)}$, and $O_{\epsilon j}^{(3)}$ to the *object wave* $O_{\epsilon j}$ arising when the origin of the surface atomic layer is at the point j at a height d above the outermost bulk atomic layer. The distribution of atoms in the surface is assumed to extend to a height h above the bulk. The plane parallel to the surface at this height contains the real-space origin O with respect to which all mutually coherent electron paths are referenced. The conventional origin for the calculation of the bulk reflection matrix \mathbf{B}^+ is assumed to be at a point B just above the outermost bulk layer.

the test overlayer, taken at the position of an atom in the test overlayer at a height d above the substrate. Take, as well, B to be the origin of the substrate defined for the creation of the bulk reflection matrix B^{-+} . We are now in a position to define propagation matrices (also in the plane wave basis) between these layers, P_{jO} is such a matrix for electron propagation from O to j . P_{Bj} is likewise defined for propagation from j to B . For propagation in the reverse direction, identically defined are P_{jB} and P_{Oj} . Bringing all of these pieces together allows us to write the total reflection matrix of the entire surface, to first order in back-scattering, as

$$T = P_{Oj} P_{jB} B^{-+} P_{Bj} P_{jO} + P_{Oj} M^{-+} P_{jO} \dots \\ + P_{Oj} (1 + M^{-}) P_{jB} B^{-+} P_{Bj} (1 + M^{++}) P_{jO} \quad (6.18)$$

where unit matrices I are added to the “in-in” and “out-out” matrices to account for unscattered transmission through the overlayer, that then may scatter from the overlayer upon reflection from the substrate, or scatter from the overlayer followed by the bulk and then pass back through the overlayer without a second interaction. Also, in actuality we take the space between the layers to have a constant potential, making the interlayer propagators free space propagators, so the product of any two is independent of an intermediate point, giving

$$P_{BO} = P_{Bj} P_{jO} \quad (6.19)$$

and

$$P_{OB} = P_{Oj} P_{jB}. \quad (6.20)$$

The first term in eq. (6.18) can then be identified as the reference wave, R_ϵ in eq. (6.2), namely:

$$\mathbf{R}_\varepsilon = \left(\mathbf{P}_{OB} \mathbf{B}^{-+} \mathbf{P}_{BO} \right)_{\mathbf{g}\mathbf{0}} \quad (6.21)$$

where the indices $\mathbf{g}\mathbf{0}$ specify scattering from the incident beam ($\mathbf{g}=\mathbf{0}$) into a beam specified by reciprocal lattice vector \mathbf{g} contained in ε . The remaining terms in eq. (6.18) give the form of the elementary object waves via:

$$\begin{aligned} \mathbf{O}_{\varepsilon j} &= \left(\mathbf{P}_{Oj} \mathbf{M}^{-+} \mathbf{P}_{jO} + \mathbf{P}_{Oj} (1 + \mathbf{M}^{-}) \mathbf{P}_{jB} \mathbf{B}^{-+} \mathbf{P}_{Bj} (1 + \mathbf{M}^{++}) \mathbf{P}_{jO} \right)_{\mathbf{g}\mathbf{0}} \\ &\simeq O_{\varepsilon j}^{(1)} + O_{\varepsilon j}^{(2)} + O_{\varepsilon j}^{(3)} \end{aligned} \quad (6.22)$$

where

$$O_{\varepsilon j}^{(1)} = \left(\mathbf{P}_{Oj} \mathbf{M}^{-+} \mathbf{P}_{jO} \right)_{\mathbf{g}\mathbf{0}}, \quad (6.23)$$

$$O_{\varepsilon j}^{(2)} = \left(\mathbf{P}_{OB} \mathbf{B}^{-+} \mathbf{P}_{Bj} \mathbf{M}^{++} \mathbf{P}_{jO} \right)_{\mathbf{g}\mathbf{0}}, \quad (6.24)$$

and

$$O_{\varepsilon j}^{(3)} = \left(\mathbf{P}_{Oj} \mathbf{M}^{-} \mathbf{P}_{jB} \mathbf{B}^{-+} \mathbf{P}_{BO} \right)_{\mathbf{g}\mathbf{0}}, \quad (6.25)$$

where the fourth term involving the product of scattering matrices \mathbf{M}^{++} and \mathbf{M}^{-} has been neglected. As result our object wave contains only terms which are first order in scattering from the test overlayer. The four scattering paths included in the composition of (6.2) are illustrated in Figure 6.1.

The scattering paths used in this approximation are actually a very good approximation for the case of an adsorbate confined to a single layer on a surface, due to the predominately forward scattering nature of atomic scattering factors. It was a little surprising when these approximations proved to be adequate, when applied in the algorithm described earlier, for the recovery of an adsorbed layer of CO oriented perpendicular to a Ni substrate.

The first application of the algorithm, including the approximations outlined above, is only meant to be a very basic “proof of concept”. Our aim is to recover the heights of the C and O atoms in an ordered $c(2 \times 2)$ overlayer on Ni(001) from a single simulated I/E curve of the (00), or specular, intensities. These intensities were calculated from standard LEED codes [Va79] over an experimentally accessible energy range. Also required for the algorithm is the reference wave R_e composed of the bulk scattering matrix B^{++} and the propagators, as well as the object wave matrices O_{ej} which require the test overlayer scattering matrices M^{++} and M^{--} and the interlayer propagators. All of these quantities are obtained from the same set of computer codes. The algorithm is

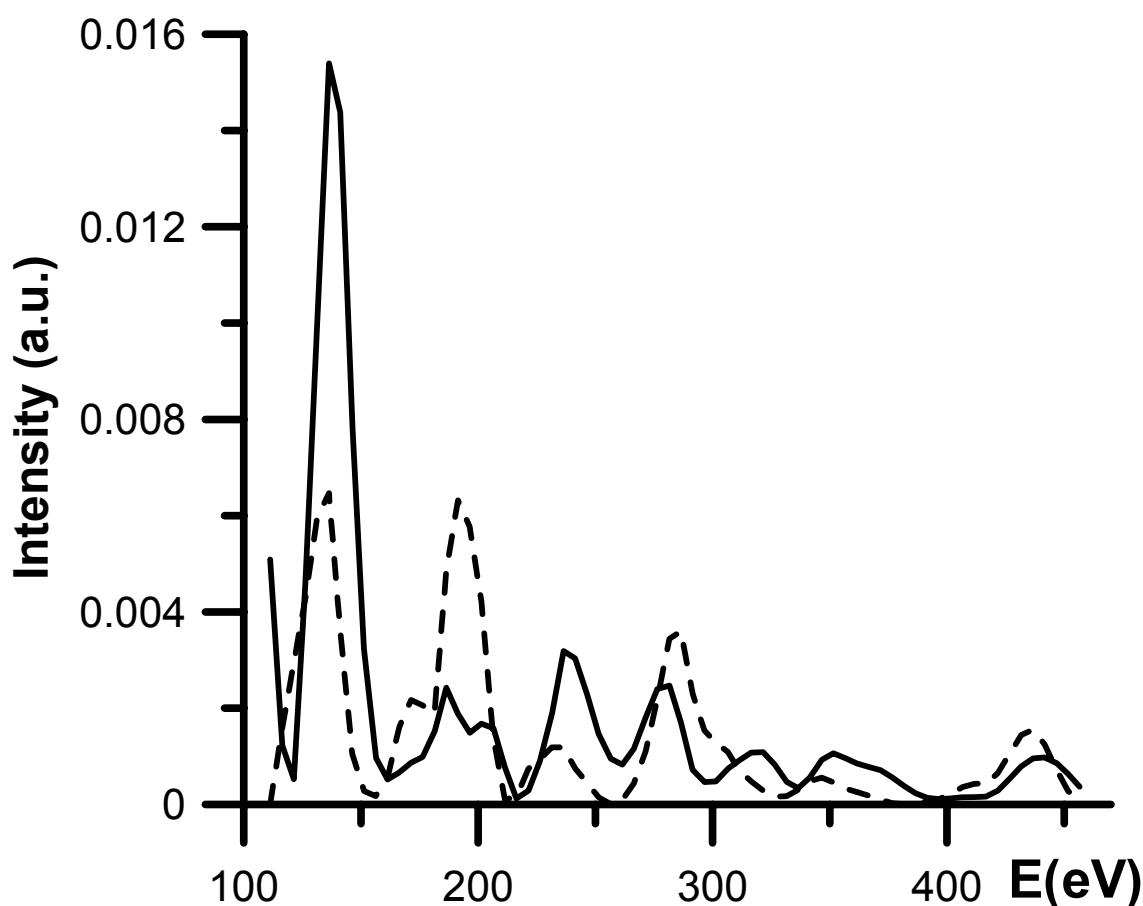


Figure 6.2 Solid line: calculated LEED intensity vs. energy for the specular, or (00) beam from a $c(2 \times 2)$ -CO/Ni(001) surface. Dashed line: calculated LEED intensity vs. energy for the same beam from a clean Ni(001) surface with the same electron absorption parameters.

initialized by taking $\{p_j^{(0)}\}$ to be a uniform distribution normalized to the suspected number of atoms in the surface unit cell. In the present case that is 1.0 per unit cell since we are using just the specular beam, we can only recover the laterally averaged distribution of atoms in the unit cell. Since the surface is $c(2 \times 2)$ and there are four atoms in total (2 CO molecules per 2×2 unit cell), the lateral average is one atom. In the general case, where more beams are being included in the calculation, the distribution would be normalized to the number of suspected atoms.

Figure 6.2 shows the calculated I/E curve (solid line), over an energy range of about 100 to 400 eV, from a $c(2 \times 2)$ -CO/Ni(001) surface. Assuming an on top adsorption site the Ni to C spacing was taken to be 1.7 Å, the C to O spacing 1.5 Å, and the height h of the origin O above the uppermost Ni layer is taken to be its known value of 3.93 Å. Also shown in Figure 6.2 is the intensity (dashed line) from a bulk terminated Ni(001) surface which is equal to the modulus squared of the complex amplitudes that represent our reference wave R_e .

A complication in the present case is that the two adsorbate atoms are of different species. It might be imagined that the theory developed above would have to be generalized to include separate spatial distributions of both the C and O, with corresponding elementary object wave matrices O_{ej} . Yet, as we shall see in the present case, it appears that the kinematic layer scattering matrices $M^{\pm\pm}$ for both C and O are sufficiently similar to permit us to use just that from one of the surface species. In this case we used just that of O.

Figure 6.3 shows the evolution of the recovered spatial distribution $\{p_j^n\}$ at different numbers of iterations. Figure 6.3a is the distribution after the first iteration,

upon having initialized the algorithm with a uniform distribution. After 500 more iterations there can already be seen significant indications of the positions of the adsorbate atoms, $\{p_j^{(500)}\}$ is shown in Figure 6.3b. The final result $\{p_j^{(3000)}\}$ after a total of 3000 iterations shown in Figure 6.3c gives a remarkably clear and accurate indication of the heights of both the C and O atoms. In practice more LEED beams are available from the experiment and can be used as input to the algorithm. This has enabled the recovery of the full three dimensional distribution of atoms in the surface [DKS02].

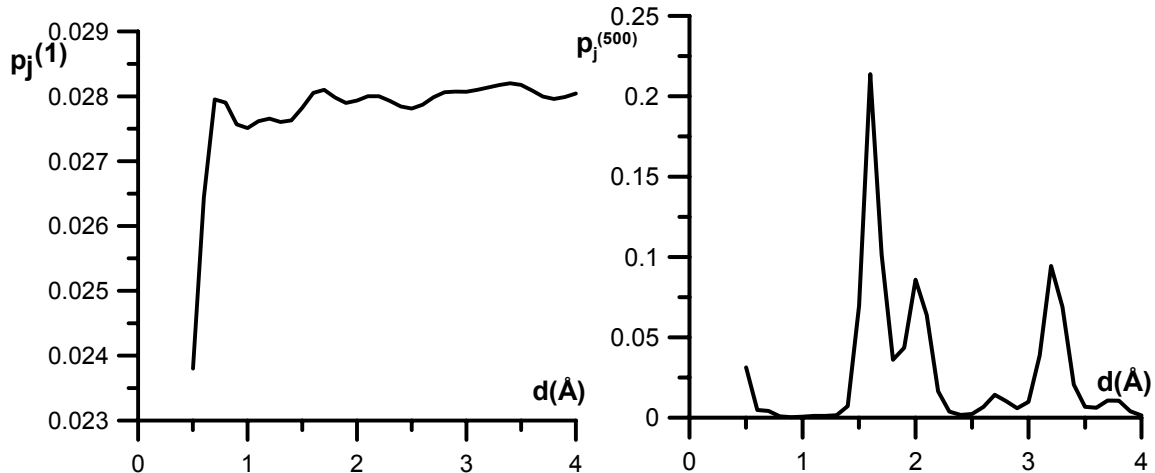


Figure 6.3a

Figure 6.3b

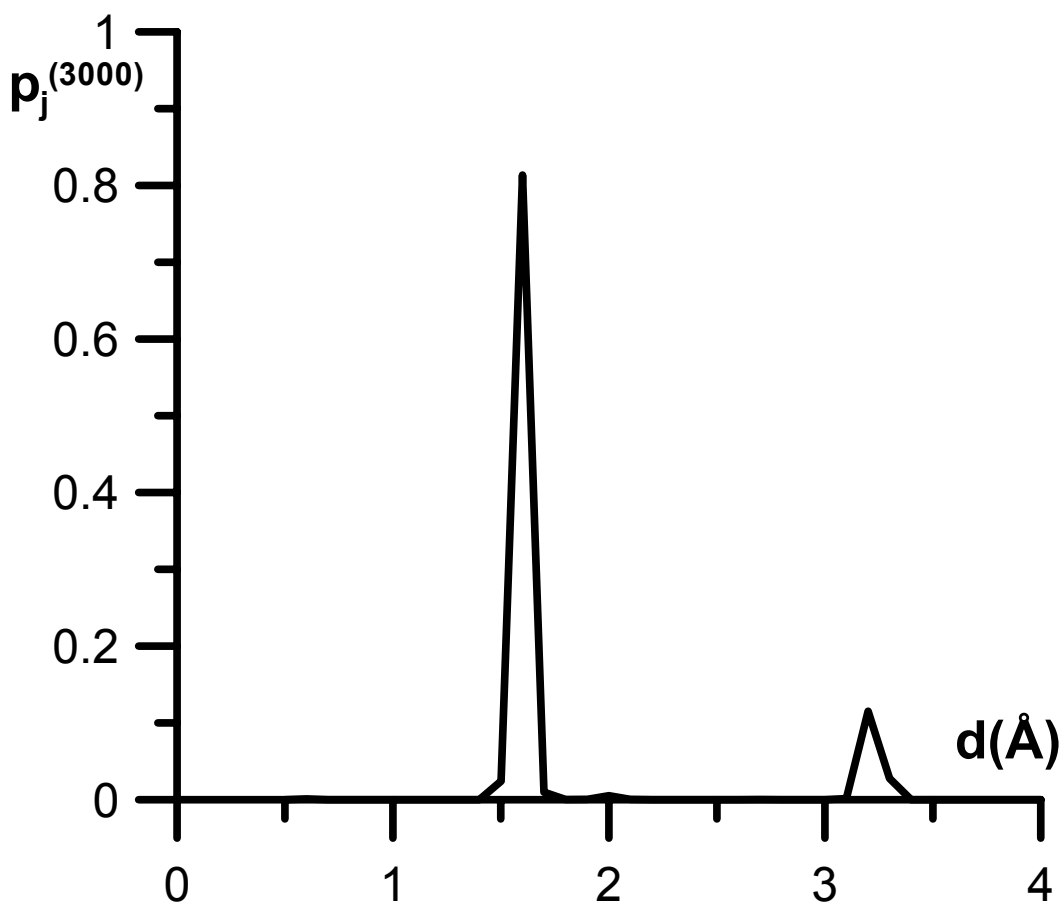


Figure 6.3c

Figure 6.3 Evolution of the one-dimensional distribution of atomic scatters as calculated by our algorithm as a function of height above the outermost layer of Ni atoms of the substrate. (a) The distribution $\{p_j^{(1)}\}$ after a single iteration (b) that $\{p_j^{(500)}\}$ after 500 iterations, and (c) that $\{p_j^{(3000)}\}$ after 3000 iterations. The final distribution correctly reproduces the heights of the C and O atoms at approximately 1.7 Å and 3.2 Å respectively.

Chapter 7: Summary, Suggested Further Work &

Conclusions

This work has shown that the maximum entropy principle of information theory, in combination with many of the tried and true phasing methods from various fields, can be assembled into an inverse method for surface x-ray diffraction, as well as low energy electron diffraction. The algorithm developed has been shown to work well at recovering the desired electron density distribution, or atom distribution in the LEED case, from just the experimentally obtained intensities of the diffraction pattern and knowledge of the bulk structure of the crystal.

Different types of surfaces have been used as test structures, through simulation of experimental intensities. The O/Cu(104) test case was an example of the algorithm's ability to recover the electron density distribution of a surface with the same periodicity as that of the bulk parallel to the surface. Given the quality of the starting phases, since the surface Cu atoms are only slightly displaced from bulk positions, it is not entirely surprising that the Cu atoms are well represented in the recovered electron density. The impressive portion of the result is in the algorithm's ability to apparently create the O atoms that are adsorbed onto the surface. The GaAs(111)-2x2 case showed the ability of the algorithm to deal with surfaces of lower periodicity than the bulk. The phases of the superstructure spots were handled well once the algorithm had suitably determined the phases of the CTRs. This example demonstrated the algorithm's ability to actually remove density from parts of the unit cell in the formation of the surface vacancy. Also

demonstrated was the ability to recover the significant relaxation of the outermost layers of Ga and As.

The first couple of examples presented were of surface structures with just a single domain. It is actually far more common to find multiple, symmetrically related, domains on a single surface. To maximize the usefulness of this algorithm it was important that it be adaptable to these structures.

Given the similarity between the mathematical expressions for the intensities from single domains and coherently averaged domains; it was not entirely surprising that the algorithm functioned as it did in the latter case. The fact the algorithm returns a superposition of the two surface domains should not be very problematic, even in the case of more realistic surface structures. Our simplified model of a dimer layer on the surface of Ge(001)-2x1 showed the capability of the algorithm to recover the surface electron density distribution from data of this type.

Usually the domains on a surface are large in comparison to the coherence length of the x-rays used in the experiment. As a result, it is more often the case that the intensities from each are averaged and not the complex amplitudes. This leads to the component termed the target function in the algorithm taking on a form in which the estimated surface structure factor from the second domain enters directly into the expression. This is in contrast to the single domain case where it contributes only through the phases of its interference with the bulk amplitudes. The fact that it did indeed recover the surface electron density, not only for the simplified Ge(001)-2x1 dimer model but also, the more realistic, yet hypothetical, c(2x2)-K/TiO₂ model was very satisfying.

It was observed that there seems to be a correlation between the ratio of superstructure spots to CTRs included in the data set, and the need to run the algorithm including just the CTRs before including the superstructure amplitudes. Further investigation of this effect is planned. It was also observed that the algorithm functions equally well in the multiple domain case regardless of whether the superstructure rods contain contributions from just one domain or both domains.

An obvious void in this work is a chapter showing results based on real experimental data. One reason for this omission is the differing requirements of the MEM algorithm developed here from that of the conventional trial-and-error fitting methods commonly employed. Our algorithm works best with a fairly complete three dimensional data set in reciprocal space. The conventional SXRD data set includes many “in-plane” reflections measured at small values of the Miller index L . Typically only a small number of “rod scans”, in which many values of L are measured for given H and K , are taken. The largely in-plane dataset is adequate for the conventional analysis because the in-plane reflections are sensitive to the variation of the structure parallel to the surface and the few rod scans lend sensitivity to the third dimension perpendicular to the surface. We have not had much success with the one example of conventional data obtained from I.K. Robinson for the O/Cu(104) structure [Wa99]. A comparable number of simulated data points are used in the example given in chapter four. The algorithm we have developed just needs them to be measured in a different fashion than is conventionally done.

Using just the in-plane reflections it should be possible to recover the two dimensional projection of the surface electron density. In an attempt to recover the

projected density the Cu atom were seen to show up, to no surprise given the initial phase estimate, but the O atoms were not confidently represented by any of the features in the result. Hopefully work will continue on adaptations of the algorithm to these more conventional data sets.

Work is in progress on data sets from Ge(001)-2x1 [LyD] and c(2x2)-K/TiO₂ [MoD]. These data sets were measured by the referenced experimenters explicitly for application of the algorithm we have developed. One of the major factors involved in application of this algorithm to experimental data is the relative scaling of the measured intensities to the calculated amplitudes of the bulk. Tests done with simulated data have shown it is sufficient to scale the experimental intensities to the calculated intensities through a simple ratio of the sums of the two during each iteration. Stating this explicitly,

$$scaled_I_q^{Exp} = \frac{\sum_q I_q^{Estimated}}{\sum_q I_q^{Exp}} I_q^{Exp} \quad (7.1)$$

where $scaled_I_q^{Exp}$ is the intensity used in the calculation of the target distribution either through its square root or directly depending on the type of data in question.

$I_q^{Estimated}$ is the estimate of the intensities obtained from the known bulk structure and the current estimate of the surface electron density distribution. I_q^{Exp} are the actual intensities obtained from the experiment. This scaling is done during each iteration, just before the reciprocal space target function is computed. If in-plane reflections are included in the data set it may be necessary to scale them independently of the rest of the data. This is due to the fact that attenuation of waves at a grazing angle to the surface is

governed by the damping length of evanescent waves in the surface region, which is much stronger [Wo94].

Another concern is the degree to which we actually know the complete bulk structure. It may be the case that the support constraint, which assumes that everything below Z equals zero is in the bulk or only contributes to the reference wave, will need to be modified so that the algorithm can modify the electron density below the surface unit cell. This would, hopefully, allow the algorithm to deal with imperfectly known bulk structure by effectively modifying the reference wave used in the algorithm.

In the theme of modifying the reference wave, in the process of solving a truly unknown surface structure, it may be the case that some atoms will be determined by an initial execution of the algorithm. It would then be good to run the algorithm again where now these “known” atoms are included in the reference wave, as another known component in addition to the truncated bulk amplitudes which are also subtracted from the experimental amplitudes in the formation of the target function of the algorithm. This may allow the algorithm to better determine the remaining surface electron density distribution. It may be the case that lighter atoms, such as oxygen, may not have shown up initially due to the relatively high electron density associated with another surface species, i.e. the copper in the O/Cu(104) example. It is possible that from the additional run of the algorithm, with the modified reference wave, the other atoms in the surface will become evident. If there are indeed no more atoms to be recovered the algorithm should essentially not change the density distribution.

The potential of this algorithm for the solution of unknown surface structures is only beginning to be explored. Its viability has been proven in numerous examples

utilizing simulated SXRD and LEED data. In fact the capability has been proven in the LEED case already [DKS02] in which the $c(2 \times 2)$ -Br/Pt(110) surface has been recovered from experimental LEED intensities. I am confident that with implementation of the ideas suggested above and continuing refinement of the programs that this method will become a powerful addition to the array of tools available for determination of the atomic structure of surfaces.

References

- [Bi85] This quasi-dynamical approximation has also been employed successfully in conventional LEED analyses; see e.g. N. Bickel and K. Heinz 1985 *Surf. Sci.* **163** 435 (1985).
- [Br84] G. Bricogne 1984 *Acta Crystallogr. A* **40** 410
- [Br88] G. Bricogne 1988 *Acta Crystallogr. A* **44** 517
- [Br91] G. Bricogne 1991 *Maximum Entropy in Action* ed B. Buck and V.A. Macaulay (Oxford University Press) p. 187
- [Co82] D.M. Collins 1982 *Nature* **298** 49
- [Coc51] W. Cochran 1951 *Acta Cryst.* **4** 408
- [DKS90] D. K. Saldin and P. L. de Andres 1990 *Phys. Rev. Lett.* **64** 1270-3.
- [DKS97] D.K. Saldin 1997 *Surface Review and Letters*, **4** 441
- [DKS02] D.K. Saldin, A. Seubert, and K. Heinz 2002 *Phys. Rev Lett* **88** 115507
- [Fi78] J.R. Fienup 1978 *Optics Lett.* **3** 27
- [Fi82] J.R. Fienup 1982 *Appl. Opt.* **21** 2768
- [Gi96] C. J. Gilmore 1996 *Acta Crystallogr. A* **52** 561
- [Gia80] C. Giacovazzo 1980 *Direct Methods in Crystallography* (London:Academic)
- [GD78] S.F. Gull and G.J. Daniell 1978 *Nature* **272** 686
- [GS71] R.W. Gerchberg, W.O. Saxton 1971 *Optik* **35** 237
- [He01] K. Heinz, A. Seubert, and D. K. Saldin, 2001 *J. Phys.: Condens. Matter* **13**, 10647-10663
- [ITXRD74] James A. Ibers and Walter C. Hamilton Editors 1974 *International Tables for X-ray Crystallography Vol. IV*
- [Ja57] E.T. Jaynes 1957 *Phys. Rev.* **106** 620
- [LyD] Data courtesy of P.F. Lyman University of Wisconsin- Milwaukee

- [ME02] R.J. Harder and D.K. Saldin 2002 *Holographic Surface Crystallography: Substrate as Reference* in M.A. Van Hove and W. Schattke (Eds.) *Solid State Photoemission and Electron Diffraction*, in press (Wiley).
- [MoD] Data courtesy of W. Moritz Institute of Crystallography and applied Mineralogy, University of Munich, Germany
- [NR92] William H. Press, Saul A. Teukolsky, William T. Vetterling, Brian P. Flannery 1992 *Numerical Recipes in Fortran: The Art of Scientific Computing Second Edition* (Cambridge University Press)
- [Pe74] J. B. Pendry 1974 *Low Energy Electron Diffraction* (Academic, London)
- [Pe88] J.B. Pendry, K Heinz, W. Oed 1988 *Phys. Rev. Lett.* **61** 2953
- [Re97] R. Read 1997 *Methods Enzymol.* **277** 110
- [Rei65] F. Reif 1965 *Fundamentals of Statistical and Thermal Physics* (McGraw-Hill)
- [Reu97] K. Reuter, J. Bernhardt, H. Wedler, J. Schardt, M. Starke, K. Heinz 1997 *Phys Rev Lett* **79** 4818
- [Ro92] I.K. Robinson & D.J. Tweet 1992 *Rep. Prog. Phys* **55** 599
- [Sa52] D. Sayre 1952 *Acta Cryst* **5** 60-65
- [Sh01] V.L. Shneerson, D.L. Wild, D.K. Saldin 2001 *Acta Cryst A* **57** 163
- [Si96] D.S. Sivia 1996 *Data Analysis: A Bayesian Tutorial* (Oxford University Press)
- [Sz93] A. Szöke 1993 *Phys. Rev. B* **47** 14044
- [To84] S.Y. Tong, G. Xu, W.N. Mei 1984 *Phys Rev Lett* **52** 1693
- [Va79] M.A. Van Hove and S.Y. 1979 Tong *Surface Crystallography by LEED* (Springer, Berlin)
- [VI98] E. Vlieg 1998 *A Concise ROD Manual* (unpublished)
- [VI00] E. Vlieg 2000 *J. Appl. Cryst.* **33** 401
- [Wa99] D.A. Walko, I.K. Robinson 1999 *Surf. Rev. Lett* **6** 851

- [Wo94] D. P. Woodruff and T.A. Delchar 1994 *Modern Techniques of Surface Science* (Cambridge University Press)

Vita

Ross J Harder

Place of birth: Los Alamos, NM

Education

B.S., University of Wisconsin-Milwaukee, December 1994
Major: Physics

M.S., University of Wisconsin-Milwaukee, December 1997
Major: Physics

Ph.D., University of Wisconsin-Milwaukee, May 2002

Dissertation Title: Phase Retrieval Methods for Surface Crystallography

Publications:

D.K. Saldin, R. Harder, V.L. Shneerson, H. Vogler, W. Moritz, in M. Benfatto, C.R. Natoli, E. Pace (Eds.), *Theory and Computation for Synchrotron Radiation Spectroscopy*, AIP Conference Proceedings, Vol. 514, American Institute of Physics, New York, 2000, p. 130

D.K. Saldin, R. Harder, H. Vogler, W. Moritz, I.K. Robinson 2001 *Comput. Phys. Commun.* **137** 12

D.K. Saldin, R. J. Harder, V.L. Shneerson, W. Moritz 2001 *J. Phys. Condens. Matter* **13** 10689

D.K. Saldin, R. J. Harder, V.L. Shneerson, W. Moritz 2001 *J. Phys. Condens. Matter* **14** 4087

R.J. Harder and D.K. Saldin 2002 *Holographic Surface Crystallography: Substrate as Reference* in M.A. Van Hove and W. Schattke (Eds.) *Solid State Photoemission and Electron Diffraction*, in press.

Contributed presentations:

American Physical Society Meeting, March 2000, "A Direct Method for Surface X-ray Diffraction"

University of Wisconsin – Milwaukee, Laboratory for Surface Studies Student Symposium, July 2001, "A Direct Method for Surface X-ray Diffraction"

University of Wisconsin – Milwaukee, Physics Department Colloquium, April 2002, "A Direct Method for Surface X-ray Diffraction"

Major Professor

Date